https://dx.doi.org/10.1016/j.electacta.2021.139196
This is the Pre-Published Version.

Phase-Field Modeling of Mechano–chemical-coupled Stress-Corrosion Cracking

Chen Lin[a], Haihui Ruan[b, *]

a. Sino-French Institute of Nuclear Engineering and Technology, Sun Yat-Sen University, Zhuhai, China

b. Department of Mechanical Engineering, The Hong Kong Polytechnic University, Hong Kong, China

Abstract

A mechano–chemical coupling phase-field model is proposed to investigate stress-corrosion cracking (SCC). It is demonstrated that pit-to-crack transition occurs when the relative-rate parameter, $\kappa_v > 1$, which characterizes the critical scenario where stress-induced degradation occurs faster than electrochemical dissolution. Moreover, an exponential relationship between the stress intensity factor and cracking velocity is revealed, and it indicates an autocatalytic process resulting from the accelerations of stress and corrosion. We provide further details regarding the variation in the electrochemical environment, effect of mechanical loading, and significant role of the initial geometry in promoting SCC. The results obtained are useful for assessing critical structures in corrosive environments.

Keyword: Phase-Field Model; Stress-Corrosion Cracking; Mechano–chemical Coupling.

* Corresponding author Tel.: + 852 2766 6648, Fax: +852 2365 4703, E-mail address: haihui.ruan@polyu.edu.hk

Introduction

Repairs and replacements caused by corrosion have resulted in significant economic burden in many countries. For example, in China, the cost incurred by corrosion amounted to approximately 3.34% of its gross domestic product (GDP in 2018 [1], which is significantly higher than the cost of all-natural disasters combined. Among various corrosion-induced failures, stress-corrosion cracking (SCC), a progressive fracture caused by stress and the electrochemical environment, has long been recognized as one of the most typical and dangerous types of localized corrosion [2]. It significantly degrades the integrity and durability of materials, thereby limiting the lifetime and reliability of key industrial equipment.

However, the mechanism of SCC, which results from the complicated conjoint actions of stress and electrochemical fields, are difficult to understand. Among the various SCC mechanisms proposed, three are refereneced the most, *i.e.*, stress-sorption [3–4], film-rupture–metal-dissolution [5–7], and hydrogen embrittlement [8–10]. The stress-sorption mechanism ascribes SCC to adsorbed specific species that interact with strained chemical bonds at crack tips, resulting in a decrease in the bond strength and surface energy, and consequently, a reduction in the stress threshold for a brittle fracture. In the film-rupture–metal-dissolution mechanism, as stress increases, a crack begins to develop at the tip of a corrosion pit, thereby destroying the passive film and exposing the fresh material to the corrosive environment. Consequently, the concentrated stresses promote the corrosion rate, and the metal dissolution results in a further increase in the stresses at the crack tip. These factors result in an

autocatalytic process, which induces material failure. In the hydrogen embrittlement mechanism, fracture occurs because of a brittle region at the crack tip caused by the entry of hydrogen. Fontana and Greene [11], however, argued that because hydrogen embrittlement is not a corrosion process, cracking occurring by this mechanism should not be considered as SCC.

In-situ experiments using scanning electron microscopy (SEM) [12, 13], synchrotron X-ray tomography [14], and the direct current potential drop (DCPD) method [15] have been conducted to observe SCC. However, these methods have limitations. For example, the DCPD method cannot directly characterize the morphology evolution of cracks, whereas SEM can only offer a limited resolution; none of these methods can quantify the stress, electric, and chemical fields inside a crack. SCC involves complex interactions among the stress state, material microstructure, and electrochemical kinetics. The effect of each individual factor is extremely difficult to experimentally differentiate and determine. Therefore, numerical approaches have become essential for reliability analysis and anticorrosion design involving SCC.

Theoretically, based on a predefined crack geometry, several analytical and numerical models [16–19] have been proposed to predict the electrochemical evolution within a crack. In these analyses, Nernst–Planck equations are employed to describe the diffusion and reaction in an electrolyte, the Laplace or Poisson equation to describe the electric field, and the flux boundary conditions imposed on the crack surfaces to account for metal dissolution. However,

when the corrosion rate is high, this type of model results in significant errors because morphology evolution is not involved.

The migration of the metal–electrolyte interface (i.e., pitting and cracking) can be resolved using the finite element method (FEM) [20–22], in which the position of the interface can be determined based on the resolved cracking velocity supplemented with a remeshing or moving-mesh technique (e.g., the arbitrary Lagrangian–Eulerian technique [23]) to accommodate sharp interfaces. However, this method often results in many numerical errors, a high computational cost, and mesh-dependent results; therefore, it is extremely difficult to apply this method to complex problems. Additionally, the cracking problem can be managed using the extended finite element method (XFEM) [24, 25]. However, the use of the XFEM for SCC renders it difficult to solve the electrochemical governing equations on new surfaces because the latter are still within the elements. Other solution approaches, such as the finite volume method [26], cellular automata [27–29], and peridynamics [30–32], are also employed in modeling corrosion; however, they are more complicated than the FEM and generally require more computational resources.

Assuming diffusive interfaces, the phase field (PF) method avoids the difficulty in accommodating moving interfaces; all governing equations become solvable when the FEM is used (e.g., a commercial FEM package). Because of the convenience of incorporating the effects of various physical, chemical, and mechanical fields, the PF method has been employed to investigate various material processes. A few PF models have been proposed to model SCC.

In an early study involving a PF model, Ståhle *et al.* [33] investigated the formation of corrosion pits, the initiation and growth of cracks, and crack branching. However, electrochemical processes, such as diffusion and reaction, were not incorporated into the model. Based on the film-rupture–metal-dissolution mechanism, Mai *et al.* [34] proposed a PF model to describe the SCC process, wherein a relationship between the stress field and interface kinetics was assumed. Considering the contributions of chemical potential and elastic energy to the free energy of an SCC system, Nguyen *et al.* [35–37] proposed another PF model, in which the material dissolution rate was correlated with the fluxes of reactants and the release of elastic energy after dissolution. In the models of Mai *et al.* and Nguyen *et al.*, corrosion was regarded as a diffusion process; hence, the reaction kinetics were not considered to be rate-limiting factors. Lin *et al.* [38, 39] formulated the reaction kinetics in the form of generalized Butler–Volmer (BV) equations in their PF models. Hence, the overpotential can be correlated with diffusivity, electric field, interfacial energy, and mechanical deformation, thereby enabling stress-assisted local corrosion and the corresponding change in an aqueous environment to be investigated.

However, to the best of our knowledge, a numerical model describing all the complexities of electrochemical and mechanical processes and their intrinsic interactions in SCC does not exist. Therefore, we herein propose a new PF model that involve the formulations of chemical potential, electrostatic potential, and mechanical and interfacial energies, whose summation represents the Helmholtz free energy of the system; furthermore, the model can accommodate

the kinetics of diffusion, metallic dissolution, and cracking. In the PF framework, we describe the cracking process using an Allen–Cahn-type equation to minimize the free energy of the system, which is consistent with the theory of strain energy release rate in fracture mechanics. The electrochemical kinetics of corrosion are described as a function of the electrochemical potentials of the reactants and products, which involves the effects of stresses, electric fields, and corrosive environments. Considering mass conservation and electroneutrality, a set of Nernst–Planck–Poisson equations with reaction kinetics as the sink/source terms are established to accommodate variations in the field variables. The proposed PF model is solvable using a commercial FEM package, which is effective for investigating SCC and the relationship between stress and corrosive species.

2. Methodology

2.1 SCC mechanism

The SCC process, as illustrated in Fig 1, begins with a local breakdown of the passive film, which exposes a fresh material into a corrosive environment, e.g., saltwater. With the applied anodic potential, denoted by φ, the metal (M) corrodes and releases metal cations (M^{n+}) into the electrolyte, whereas is releases electrons (e^-) into the metallic electrode, as follows:

$$M \rightarrow M^{n+} + ne^- . \quad (1)$$

When the metallic component is under mechanical loading, the stress concentration at the tip of a corrosion pit accelerates local corrosion [38–42], resulting in the sharpening of the

corrosion pit [38, 39, 43, 44]. This yields a higher stress concentration, a higher anodic dissolution rate, and an autocatalytic process of crack propagation until catastrophic failure occurs.

Fig. 1

2.2. Thermodynamics

We begin by introducing a general expression of the Helmholtz free energy, denoted by Ψ, which is an integral of the density functional, ψ, over the domain, Ω, for a dissipative system, as follows:

$$\Psi = \int_{\Omega} \psi dv = \int_{\Omega} \left(\psi^{\text{chem}} + \psi^{\text{elec}} + \psi^{\text{mech}} + \psi^{\text{int}} \right) dv \,. \tag{2}$$

As expressed in Eq. (2), the density functional ψ is expressed as four terms describing the chemical, electric, mechanical, and interfacial potentials (ψ^{chem}, ψ^{elec}, ψ^{mech}, and ψ^{int}, respectively).

Using saltwater as an example electrolyte, the diffusible species are M^{n+}, Cl^-, and Na^+, whose concentrations are denoted by $c_{M^{n+}}$, c_{Cl^-} and c_{Na^+}, respectively. The chemical energy density ψ^{chem} is expressed as follows:

$$\psi^{\text{chem}} = \sum\nolimits_{*} \psi_{*}^{\text{chem}} \left(c_{*} \right) \left(* = \text{M}^{n+}, \text{Na}^{+}, \text{Cl}^{-} \right), \tag{3}$$

where ψ_{*}^{chem} is the chemical energy density, where the subscript denotes the type of diffusible ion *. Because M^{n+}, Na^+, and Cl^- only exist in the electrolyte, ψ_{*}^{chem} is defined based on a dilute solution, as follows:

$$f_{*}^{\text{chem}} = c_{*} RT \left(\ln \bar{c}_{*} - 1 \right) + c_{*} \mu_{*}^{0} \quad \left(* = \text{M}^{n+}, \text{Na}^{+}, \text{Cl}^{-} \right), \tag{4}$$

where μ_*^0, R, and T are the standard chemical potential, ideal gas constant, and thermodynamic temperature, respectively; $\bar{c}_* = c_* / c_*^{\mathrm{ref}}$ is the dimensionless concentration with c_*^{ref} being the saturated concentration of ion *.

The electric potential energy density, ψ^{elec}, resulting from the charge density, is expressed as

$$\psi^{\mathrm{elec}} = F\left(n\varphi_{\mathrm{L}} c_{\mathrm{M}^{n+}} + \varphi_{\mathrm{L}} c_{\mathrm{Na}^{+}} - \varphi_{\mathrm{L}} c_{\mathrm{Cl}^{-}} - \varphi_{\mathrm{S}} c_{\mathrm{e}^{-}}\right), \tag{5}$$

where F, φ_{S}, and φ_{L} are the Faraday constant and electrostatic potential in the metallic electrode and electrolyte, respectively. Because metal is a conductor, the distribution of φ_{S} is assumed to be uniform, with the magnitude being either zero (grounded) or an applied potential difference.

Considering elastoplastic deformation, the mechanical energy density ψ^{mech} can be written as the sum of the elastic and plastic contributions, as follows:

$$\psi^{\mathrm{mech}} = \psi^{\mathrm{elas}} + \psi^{\mathrm{plas}}, \tag{6}$$

where the elastic term, employing the assumption of linear elasticity, is expressed as

$$\psi^{\mathrm{elas}} = p(\phi)\frac{1}{2}\left(\left(\boldsymbol{\varepsilon}^{\mathrm{e}}\right)^{T} \cdot \left(\mathbf{D}^{\mathrm{e}}\boldsymbol{\varepsilon}^{\mathrm{e}}\right)\right). \tag{7}$$

Here, $\mathbf{D}^{\mathrm{e}}$ and $\boldsymbol{\varepsilon}^{\mathrm{e}}$ are the stiffness matrix and elastic strain tensor of the metallic electrode, respectively. In Eq. (7), a function $p(\phi)$ is used to mollify the discontinuity from the solid to the liquid phase, as mechanical deformation only occurs in the solid. Using $p(\phi)$ is a fundamental technique in the PF model. In this study, $p(\phi)$ is a Hermitian interpolation function, i.e., $p(\phi) = \phi^3\left(10 - 15\phi + 6\phi^2\right)$ (on the other forms of $p(\phi)$, cf. the discussion in [45]) with ϕ

$\in$ [0, 1] being the order parameter of phase identification. In the present model, ϕ = 1 indicates the M phase, which can signify $\phi = c^{\mathrm{M}} / c_{\mathrm{ref}}^{\mathrm{M}}$, i.e., the normalized concentration of M in the metal anode is unity. Accordingly, ϕ = 0 indicates the liquid electrolyte (no metallic atoms, only ions), and 0 < ϕ < 1 is in the interface, in which the reaction shown by Eq. (1) occurs.

The elastic strain is expressed as

$$\boldsymbol{\varepsilon}^{\mathrm{e}} = \boldsymbol{\varepsilon} - \boldsymbol{\varepsilon}^{\mathrm{p}}, \tag{8}$$

where $\boldsymbol{\varepsilon}$ and $\boldsymbol{\varepsilon}^{\mathrm{p}}$ are the total and plastic strain tensors, respectively. We apply a linear isotropic hardening law with the von Mises yield criterion to describe the plastic deformation, which results in the following incremental expression of the plastic strain:

$$d\boldsymbol{\varepsilon}^{\mathrm{p}} = d\varepsilon_{\mathrm{eq}}^{\mathrm{p}} \frac{\partial \sigma_{\mathrm{eq}}}{\partial \boldsymbol{\sigma}}, \tag{9}$$

where $d\varepsilon_{\mathrm{eq}}^{\mathrm{p}}$ is the incremental equivalent plastic strain, $\boldsymbol{\sigma}$ is the stress tensor, and σ_{eq} is the equivalent (von Mises) stress, i.e., $\sigma_{\mathrm{eq}} = \sqrt{3/2\,\mathbf{s}:\mathbf{s}}$, with $\mathbf{s} = \boldsymbol{\sigma} - \mathrm{tr}(\boldsymbol{\sigma})/3\mathbf{I}$. Here, $\mathbf{s}$ is the deviatoric stress tensor, tr(·) is used to obtain the trace of a tensor, and $\mathbf{I}$ is the identity tensor. The corresponding plastic energy density ψ^{plas} can be expressed as

$$\psi^{\mathrm{plas}} = p(\phi)\left(\sigma_{\mathrm{y}}^{0} + \frac{1}{2} H \varepsilon_{\mathrm{eq}}^{\mathrm{p}}\right)\varepsilon_{\mathrm{eq}}^{\mathrm{p}}, \tag{10}$$

where σ_{y}^{0} and H are the initial yield strength and hardening rate, respectively.

The last energetic term in Eq. (2) is the interface energy density ψ^{int}, which represents the additional energy due to the creation of new surfaces (e.g., cracking). It is expressed as

$$\psi^{\text{int}} = Wg(\phi) + \frac{\lambda}{2}|\nabla\phi|^2 . \quad (11)$$

In Eq. (11), the first term on the right-hand side is a double-well function comprising $g(\phi) = (\phi)^2(1-\phi)^2$ and the energy barrier, W, to ensure that both the electrode (ϕ = 1) and electrolyte phases (ϕ = 0) are stable; meanwhile, the second term is the gradient energy density owing to the requirement of diffusive interfaces in a PF model [45], where λ is a constant to scale the magnitude of the gradient energy density. The two scaling factors W and λ can be correlated based on the variational principle proposed in classical fracture mechanics (i.e., the Griffith criterion is fulfilled) [46], as follows:

$$W = \frac{g_c}{2l}, \quad (12a)$$

$$\lambda = g_c l . \quad (12b)$$

In Eq. (12), g_c is the Griffith energy density, i.e., the energy dissipated upon the creation of a unit on the fracture surface; l denotes the thickness of the interface between the electrode and electrolyte, and it can be regarded as a pure numerical parameter or an actual material parameter, i.e., l can be determined from experiments (cf. [47]). However, although l should be minimal such that a fracture process can be approximated well, in a numerical implementation, l determines the mesh size, where a smaller l results in a higher computational cost.

In classical PF models [38, 39], W is correlated with λ [38], [39]. By introducing the interface energy density, s, and interface thickness, δ, W can be expressed as

$$W = 18\frac{s}{\delta}, \quad (13a)$$

$$\lambda = s\delta . \tag{13b}$$

In this case, the interface energy density, *s*, is the amount of energy released upon the creation of a new surface owing to an electrochemical process or phase transformation. Eqs. (12) and (13) are similar, although they imply different physical processes. Considering that the surface energy due to fracture is much larger than that due to corrosion, because the discontinuity caused by fracture is more abrupt, we used Eq. (12), which contains g_c and l, in the remainder of our study.

Mechano–electrochemical corrosion kinetics

For a generalized reaction, $\sum n_i \mathrm{R}_i^{X_i} \rightarrow \sum m_j \mathrm{P}_j^{Z_j}$, the reaction rate, denoted by *r*, can be defined as

$$r = -\frac{1}{n_i}\frac{\partial c_{\mathrm{R}_i^{X_i}}}{\partial t} = \frac{1}{m_j}\frac{\partial c_{\mathrm{P}_j^{Z_j}}}{\partial t}, \tag{14}$$

where R_i and P_j denote the reactants and products, respectively; n_i (or m_j) and X_i (or Z_j) are the stoichiometric number and charge number, respectively. We express *r* as follows (see our previous papers [38, 39] or Appendix A for derivation):

$$r = \frac{k^0}{a^{\mathrm{TS}}}\left(a_{\mathrm{R}} \exp\left(\frac{(1-\rho)\left(\mu_{\mathrm{R}}^{\mathrm{ex}} - \mu_{\mathrm{P}}^{\mathrm{ex}}\right)}{RT} \right) - a_{\mathrm{P}} \exp\left(-\frac{\rho\left(\mu_{\mathrm{R}}^{\mathrm{ex}} - \mu_{\mathrm{P}}^{\mathrm{ex}}\right)}{RT} \right) \right). \tag{15}$$

In Eq. (15), k^0 is the rate coefficient; a^{TS} is the activity of the reaction in the transition state (a constant in the present study); $\rho \in (0, 1)$ is the asymmetry parameter [48]; a_{R} and a_{P} are the activities of the reactants and products, respectively; $\mu_{\mathrm{R}}^{\mathrm{ex}}$ and $\mu_{\mathrm{P}}^{\mathrm{ex}}$ are the excess chemical

potentials of the reactants and products, respectively.

For oxidation, M $\rightarrow$ M^{n+} + ne^- (Eq. (1)), the activities a_R and a_P, and the excess chemical potential difference, $\mu_R^{ex} - \mu_P^{ex}$, can be expressed as

$$a_R = \exp\left(\frac{1}{RTc_M^{ref}}\left(W\frac{\partial g}{\partial \phi} - \lambda\nabla\phi^2\right)\right), \tag{16a}$$

$$a_P = \bar{c}_{M^{n+}}, \tag{16b}$$

$$\mu_R^{ex} - \mu_P^{ex} = -\mu_{M^{n+}}^0 + nF\left(\varphi_S - \varphi_L\right) + \frac{\partial p(\phi)}{c_M^{ref}\partial\phi}\left(\frac{1}{2}\left(\boldsymbol{\varepsilon}^e\right)^T\cdot\left(\mathbf{D}^e\boldsymbol{\varepsilon}^e\right) + \left(\sigma_y + \frac{1}{2}H\varepsilon_{eq}^p\right)\varepsilon_{eq}^p\right). \tag{16c}$$

Considering an enhanced mechano–chemical coupling (MCC) in solid, Gutman [49] suggested an additional term for the chemical potential, i.e., $\Delta\mu \approx V_M P$, with V_M and P the molar volume and pressure, respectively. Because experiments show that tension and compression both increase the chemical potential of solid materials [40, 42], we define $P = \left|tr\left(\boldsymbol{\sigma}\right)\right|/3$. Following Gutman [49], the effect of plastic deformation on corrosion due to the multiplication of dislocation can be incorporated by adding another term in the form of $RT\ln\left(\alpha\upsilon\varepsilon_{eq}^p/N_0 + 1\right)$, where α is a coefficient, υ an orientation-dependent factor in the range of 0.4–0.5 [50], and N_0 the initial dislocation density prior to plastic deformation. Therefore, Eq. (16c) can be rewritten as

$$\mu_1^{ex} - \mu_2^{ex} = -\mu_{M^{n+}}^0 + nF\left(\varphi_S - \varphi_L\right) + \frac{\partial p(\phi)}{c_M^{ref}\partial\phi}\left(\frac{1}{2}\left(\boldsymbol{\varepsilon}^e\right)^T\cdot\left(\mathbf{D}^e\boldsymbol{\varepsilon}^e\right) + \left(\sigma_y + \frac{1}{2}H\varepsilon_{eq}^p\right)\varepsilon_{eq}^p\right) + \frac{V_M}{3}\left|tr\left(\boldsymbol{\sigma}\right)\right| + RT\ln\left(\frac{\alpha\upsilon\varepsilon_{eq}^p}{N_0} + 1\right). \tag{17}$$

In fact, the reaction rate equation (Eq. (15)) can be rewritten in the form of the BV equation,

in which the overpotential depends on the diffusivity, electric field, interfacial energy, and mechanical stress (see our previous papers [38, 39] or Appendix B).

2.4. Governing equations

During electrochemical corrosion, the mass conservation laws for the reactants and products result in the following expression:

$$\int_{\Omega} \frac{\partial c_*}{\partial t} d\omega = -\int_{\partial\Omega} \mathbf{j}_* \cdot \mathbf{n} da + \int_{\Omega} r_* d\omega, \tag{18}$$

where $\mathbf{j}_*$ is the molar flux of species $*$ per unit area, and $\mathbf{n}$ is the outward unit vector normal to the boundary surface $\partial\Omega$. The terms on the right-hand side of Eq. (18) represent two approaches in which the concentration of $*$ can be altered, i.e., diffusion across the boundary $\partial\Omega$ (the first term) and consumption (or production) resulting from the reaction (the second term). Using Gauss's divergence theorem, the mass-conservation equation (Eq. (18)) can be expressed in differential form as follows:

$$\frac{\partial c_*}{\partial t} = -\nabla \mathbf{j}_* + r_*. \tag{19}$$

Using the Onsager linear law [51], $\mathbf{j}_*$ can be expressed as

$$\mathbf{J}_* = -\left(D_* \nabla c_* + \frac{D_*}{\delta^2\Psi/\delta {c_*}^2} \frac{\delta^2\Psi}{\delta c_* \delta\phi} \nabla\phi + \frac{D_*}{\delta^2\Psi/\delta {c_*}^2} \frac{\delta^2\Psi}{\delta c_* \delta\varphi} \nabla\varphi \right). \tag{20}$$

Using Eqs. (2) and (20), the governing equation of each concentration can be expressed as

$$\frac{\partial c_{\mathrm{M}}}{\partial t} = \nabla\left(D_{\mathrm{M}} \nabla c_{\mathrm{M}} + \frac{D_{\mathrm{M}}}{\partial^2 \psi^{\mathrm{chem}}/{c_{\mathrm{M}}}^2} \frac{\partial^2 \psi^{\mathrm{chem}}}{\partial\phi \partial c_{\mathrm{M}}} \nabla\phi \right) - r, \tag{21a}$$

$$\frac{\partial c_{\mathrm{M}^{n+}}}{\partial t} = \nabla\left(D_{\mathrm{M}^{n+}} \nabla c_{\mathrm{M}^{n+}} + n \frac{D_{\mathrm{M}^{n+}} c_{\mathrm{M}^{n+}} F}{RT} \nabla\varphi_{\mathrm{L}} \right) + r, \tag{21b}$$

$$\frac{\partial c_{\mathrm{Cl}^-}}{\partial t} = \nabla\left(D_{\mathrm{Cl}^-}\nabla c_{\mathrm{Cl}^-} - \frac{D_{\mathrm{Cl}^-}c_{\mathrm{Cl}^-}F}{RT}\nabla\varphi_{\mathrm{L}} \right), \text{ and} \tag{21c}$$

$$\frac{\partial c_{\mathrm{Na}^+}}{\partial t} = \nabla\left(D_{\mathrm{Na}^+}\nabla c_{\mathrm{Na}^+} - \frac{D_{\mathrm{Na}^+}c_{\mathrm{Na}^+}F}{RT}\nabla\varphi_{\mathrm{L}} \right). \tag{21d}$$

As SCC generally involves a significant amount of time, electroneutrality in the electrolyte can be assumed, which results in zero net flow of charges and a zero net charge density in the electrolyte. The first condition is expressed as follows:

$$\sum\nolimits_{*} \mathbf{i}_{*} = 0 \ \left(* = \mathrm{M}^{n+}, \mathrm{Na}^{+}, \mathrm{Cl}^{-} \right), \tag{22}$$

where $\mathbf{i}_{*}$ is the flow of charges transported by the diffusion flux of ions $*$, expressed as

$$\mathbf{i}_{*} = Fn_{*}\left(D_{*}\nabla c_{*} + n_{*}\frac{D_{*}c_{*}F}{RT}\nabla\varphi_{\mathrm{L}} \right). \tag{23}$$

The second condition is expressed as

$$\sum\nolimits_{*} n_{*}c_{*} = 0, \ \left(* = \mathrm{M}^{n+}, \mathrm{Na}^{+}, \mathrm{Cl}^{-} \right). \tag{24}$$

Eqs. (21–24), combined with the boundary conditions, yield the solution of the electric potential in the electrolyte φ_{L}. It is noteworthy that φ_{L} is generally non-uniform because of the difference in the mobilities of different types of ions; even in the absence of an externally applied electric field, the latter still results in the accumulation of an electric field.

Because both cracking and corrosion change the interface area, the migration rate of the electrode–electrolyte interface, delineated by the variation rate of the order parameter, $\partial\phi/\partial t$, can be segregated into two terms, as follows:

$$\frac{\partial\phi}{\partial t} = \left(\frac{\partial\phi}{\partial t}\right)_{\mathrm{c}} + \left(\frac{\partial\phi}{\partial t}\right)_{\mathrm{r}}. \tag{25}$$

The first term on the right-hand side of Eq. (25) describes cracking under mechanical loading, which can be expressed in the form of the classical Allen–Cahn equation, as follows:

$$\begin{aligned}\left(\frac{\partial \phi}{\partial t}\right)_{\mathrm{c}} &= -M_{\phi}\frac{\delta \Psi}{\delta \phi} \\ &= M_{\phi}\left(\lambda \nabla^2 \phi - W\frac{\partial g(\phi)}{\partial \phi}\right) - M_{\phi}\frac{\partial p(\phi)}{\partial \phi}\left(\frac{1}{2}\left(\boldsymbol{\varepsilon}^{\mathrm{e}}\right)^{T}\cdot\left(\mathbf{D}^{\mathrm{e}}\boldsymbol{\varepsilon}^{\mathrm{e}}\right) + \left(\sigma_{\mathrm{y}} + \frac{1}{2}H\varepsilon_{\mathrm{eq}}^{\mathrm{p}}\right)\varepsilon_{\mathrm{eq}}^{\mathrm{p}}\right)\end{aligned}, \quad (26)$$

where M_{ϕ} is the interfacial mobility. The second term on the right-hand side of Eq. (25) represents the electrode dissolution induced by corrosion. Based on our previous study [38], its evolution is associated with the corrosion reaction rate, which is expressed as follows:

$$\begin{aligned}\left(\frac{\partial \phi}{\partial t}\right)_{\mathrm{r}} &= -\frac{\partial p(\phi)}{\partial \phi}\frac{r}{c_{\mathrm{M}}^{\mathrm{ref}}} \\ &= -\frac{\partial p(\phi)}{\partial \phi}L^{\mathrm{bulk}}\left(a_{\mathrm{R}}\exp\left(\frac{(1-\rho)\left(\mu_{\mathrm{R}}^{\mathrm{ex}} - \mu_{\mathrm{P}}^{\mathrm{ex}}\right)}{RT}\right) - \overline{c}_{\mathrm{M}^{n+}}\exp\left(-\frac{\rho\left(\mu_{\mathrm{R}}^{\mathrm{ex}} - \mu_{\mathrm{P}}^{\mathrm{ex}}\right)}{RT}\right)\right)\end{aligned}, \quad (27)$$

where the function $\partial p(\phi)/\partial \phi$ (nonzero in the interfaces) is used to ensure that the electrochemical process occurs only at the electrode–electrolyte interface, and $L^{\mathrm{bulk}} = k_0/\left(a_{\mathrm{TS}}c_{\mathrm{M}}^{\mathrm{ref}}\right)$ regulates the contribution of corrosion kinetics to interface migration. Using Eqs. (26) and (27), Eq. (25) can be written as

$$\begin{aligned}\frac{\partial \phi}{\partial t} = {} & M_{\phi}\left(\lambda \nabla^2 \phi - W\frac{\partial g(\phi)}{\partial \phi}\right) - \frac{\partial p(\phi)}{\partial \phi}M_{\phi}\left(\frac{1}{2}\left(\boldsymbol{\varepsilon}^{\mathrm{e}}\right)^{T}\cdot\left(\mathbf{D}^{\mathrm{e}}\boldsymbol{\varepsilon}^{\mathrm{e}}\right) + \left(\sigma_{\mathrm{y}} + \frac{1}{2}H\varepsilon_{\mathrm{eq}}^{\mathrm{p}}\right)\varepsilon_{\mathrm{eq}}^{\mathrm{p}}\right) - \\ & \frac{\partial p(\phi)}{\partial \phi}L^{\mathrm{bulk}}\left(a_{\mathrm{R}}\exp\left(\frac{(1-\rho)\left(\mu_{\mathrm{R}}^{\mathrm{ex}} - \mu_{\mathrm{P}}^{\mathrm{ex}}\right)}{RT}\right) - \overline{c}_{\mathrm{M}^{n+}}\exp\left(-\frac{\rho\left(\mu_{\mathrm{R}}^{\mathrm{ex}} - \mu_{\mathrm{P}}^{\mathrm{ex}}\right)}{RT}\right)\right)\end{aligned}. \quad (28)$$

Eq. (28) shows that mechanical stresses result in cracking (the second term on the right-hand side) and accelerated corrosion (the third term on the right-hand side). In addition, the local stress increases at an accelerated rate with the initiation and propagation of cracks. These two

effects are not the simple superposition shown in Eq. (28), as indicated by the numerical results to be presented in the following section. It is noteworthy that the proposed model is different from the existing PF models proposed by Mai *et al.* [34] and Nguyen *et al.* [35–37]. In their models, the reaction kinetics are not formulated; therefore, a simulated corrosion process can only be diffusion mediated. In addition, their models do not include the flow of electricity; as such, the electrochemical process is difficult to describe.

3. Numerical results and discussion

To solve the governing equations above and present a detailed SCC process, we considered a two-dimensional (2D) domain measuring 100/μm × 1250/μm, which comprises a metallic electrode and an electrolyte measuring 100/μm × 150/μm and 100/μm × 1100/μm, respectively. Between the electrode–electrolyte binary system, a passive film with a thickness of 0.5/μm was assumed; the film had a local breakdown with a triangular pit, representing a surface notch (e.g., caused by scratch). Owing to symmetry, only half of the electrode–electrolyte system was modeled, as shown in Fig. 2(a). It is noteworthy that if the passive film is removed and the pit is flat, then the model reduces to a one-dimensional (1D) problem, which can be employed to verify the governing equations and the code by comparing the results with the experimental data of homogenous corrosion [52].

Fig. 2

Initially, the two phases were separated with $\phi = 1$ for the electrode and $\phi = 0$ for the

electrolyte. The zero-flux condition for the order parameter, $\nabla\phi = 0$, was applied to all sides of the domain. The initial concentrations in the electrolyte and the far field (i.e., the top boundary) were set as c_{Na^+} = 1/mol L^{-1} and c_{Cl^-} = 1/mol L^{-1}. For the other sides, zero-flux conditions, $\nabla\mathbf{c}=0$, were applied. For the electrical potential, the Dirichlet boundary conditions $\varphi_L = 0$ and $\varphi = \varphi_M$ were set at the top of the electrolyte and the bottom of the electrode, respectively; the zero-flux condition, $\nabla\varphi=0$, was applied to the other sides. The passive film was assumed to be a zero-flux boundary for the phase order parameter, ϕ, concentrations, c_*, and electrical field, φ. In terms of mechanical boundary conditions, the top of the metal was unconstrained; the bottom and right sides were constrained along their normal direction, and the left side was subjected to uniaxial tension under a constant traction, F_x, or a displacement, u_x. The reference temperature was 15/°C in the simulations.

The parameters used in the simulations are listed in Table 1. The COMSOL Multiphysics® modeling software [53] was employed to solve the proposed PF model. To guarantee the convergence of the solution and achieve a reasonable computational efficiency, the simulation domain was segregated into two regions, as shown in Fig. 2(b). Region I contains both the metallic region and the electrolyte, wherein a uniform square mesh with an element size of 0.5/μm (i.e., five times smaller than the interface thickness) was adopted because the migration of interfaces must be accurately described in this region. Region II is the far-field electrolyte, and a uniform square mesh with a larger size of 2.5/μm was adopted to solve the ion diffusion. Triangular elements with a maximum size of 2.5/μm were used to mesh the transition region

between Region I and Region II. The nonlinear governing equation were solved using the Newton–Raphson method in COMSOL, in which the time-step was automatically refined to ensure the convergence of the solution step. In our simulations, the initial and maximum time steps were $t_{ref}/2000$ and $t_{ref}/100$ for temporal integration, respectively, and they were sufficiently small to ensure a stable solution, where t_{ref} is the reference time. The evolution of the reciprocal of the time step with the step number is plotted in Fig. C.1, which shows a rapid decrease in the reciprocal of the time step from 5000 to $100/t_{ref}^{-1}$, demonstrating the stability of the nonlinear solution.

Table 1

3.1. Numerical verification: homogenous corrosion simulation (without stress)

Fig. 3

By setting the mechanical loading as zero, a 1D numerical simulation of homogeneous corrosion was first conducted to validate our model. Based on the experiments of electrochemical corrosion of a type of stainless steel [52], the applied electrode potential, φ_M, was set from -0.4 to -0.25/V, which required the critical concentration, $\bar{C}_{M^{n+}}^{cr}$, to be in the range of 7.6×10^6–1.1×10^{12}. Such a high concentration results in a high local (in the pit) M^{n+} concentration. Therefore, the corrosion process is mediated by reaction kinetics, and the corrosion rate (i.e., the velocity of interface migration), denoted by v_c, is constant for a specified potential, φ_M. This relationship, as shown in Fig. 3, agrees well with the experimental data [52]. In addition, this type of evolution is consistent with the 1D analytical solution

expressed in Eq. (C4). The numerical results show two different characteristic regimes. When the applied potential was low, the corrosion rate was linearly related to φ_M, which is the Tafel law; as φ_M increased, the v_c–φ_M relationship became exponential gradually.

Fig. 4

The 2D simulation of pitting can be (qualitatively) verified. Herein, we consider a small applied potential, φ_M = -0.6/V, which requires a low critical concentration $\bar{C}_{M^{n+}}^{cr}$ = 1. To describe the relative importance between the reaction and diffusion, we use the dimensionless Damkohler number, D_a, which is expressed as [54]

$$D_a = \frac{\left(c_M^{ref} / c_{M^{n+}}^{ref}\right) L^{bulk} l}{D^L / L}, \tag{32}$$

where L = 1250/μm is the distance between the metallic surface and the far-field boundary of the electrolyte. The variation in D_a is selected from the range of 0.27–2.7 with the change in the kinetics coefficient, L^{bulk}, from 0.003 to 0.03/s^{-1}. Fig. 4(a) shows the variation in the pit depth, d_c, with time for D_a = 0.27, 0.81, and 2.7. For a small D_a (= 0.27), d_c increased linearly with time, indicating that the corrosion process was mediated by the reaction kinetics. As D_a increased, the cation (M^{n+}) concentration at the corroded surface accumulated, thereby decelerating the reaction and resulting in a transition from kinetics- to diffusion-mediated corrosion. When D_a = 2.7, the increase in d_c became parabolic, which is consistent with the experimental observations [55] and analytical solutions [56]. The sensitivity of corrosion to D_a was further investigated based on the evolution of d_c at 100/min as a function of D_a, as plotted in Fig. 4(b). An approximate power-law relationship between d_c and D_a was revealed.

Fig. 4(c) shows further increases in the concentrations of cations M^{n+} and Cl^- anions at the tip of the pit. Because the diffusion pathway was constrained by the passive film, the locally released metallic cations could not fully diffuse into the environment, thereby resulting in a rapid accumulation near the tip of the pit. In addition, a rapid increase in c_{Cl^-} was observed, as shown in Fig. 4(c), because the transport of Cl^- anions from the outside neutralized the positive charges of M^{n+}. When the dimensionless D_a value was low (= 0.27), the increases in the cation and anion concentrations were more significant because of the longer diffusion time. The accumulation of M^{n+} near the tip of the pit resulted in an increase in the electrolyte potential φ_L. Correspondingly, the electric potential difference $\varphi_S - \varphi_L$ decreased, resulting in a gradual deceleration of pitting, as observed in experiments [57]. The increase in φ_L for different D_a values is shown in Fig. 4(d). When the D_a value was low (= 0.27), the kinetics-mediated corrosion process resulted in a gradual increase in φ_L. When the D_a value was high (= 2.7), the corrosion process was diffusion mediated and accompanied by a rapid surge in electric potential followed by a slow descent and then a plateau.

3.2. MCC in SCC

Fig. 5

Next, we consider a scenario where the metallic electrode is subject to uniaxial traction, F_x = 140–160/MPa, which induces SCC from the predefined triangular pit. The applied electrode potential, φ_M, was set as -0.1/V, and the kinetics coefficient, L^{bulk}, was set as $1.5 \times 10^{-7}/s^{-1}$ (as listed in table 1). Based on the analysis presented in the previous section, such a

low L^{bulk} resulted in a kinetics-mediated corrosion process in the absence of mechanical loading and a semicircular pit (Fig. 4(b)). With mechanical loading, a crack developed, as shown in Fig. 5(a), wherein the evolution of equivalent stress field is presented. The variations in the crack depth, d_c, and the width of the pit (i.e., opening), w_c, as defined in Fig. 5(a), are plotted in Fig. 5(b). It was observed that d_c increased at an accelerated rate because the stress concentration at the tip of the pit not only induced damage (as expressed in Eq. (26)), but also promoted corrosion by shifting the equilibrium electropotential (as expressed in Eq. B1), resulting in the initiation of a crack. Owing to the crack, a higher stress concentration was generated, and the cracking proceeded more rapidly upon the actions of stress and corrosion (i.e., the autocatalytic effect). Meanwhile, the stress magnitude (i.e., the von Mises equivalent stress) along the cracked surface was small, and the corrosion remained kinetics mediated; therefore, the variation in w_c was linear, as indicated by the dashed lines in Fig. 5(b).

Because the present PF model can predict the entire process beginning from the growth of the corrosion pit to the pit-to-crack transition and finally to the crack propagation (as shown in Fig. 5(a)), some key questions pertaining to SCC may be answered. Next, we investigate (*i*) the critical condition for the pit-to-crack transition, (*ii*) the relationship between stress and SSC velocity, and (*iii*) the effect of stress on the electrochemical environment within the crack. It is noteworthy that in previous studies involving PF models [34–37], a quantitative comparison with experimental results (e.g., polarization curves) was difficult (if not impossible). However, using our model, quantitative analysis becomes straightforward, and the critical condition for

the exponential development of SCC is relevant to that of an actual scenario.

Fig. 6

To identify quantitatively the critical condition for pit-to-crack transition, the rate difference between SCC and mere corrosion can be defined as $\kappa_v = (v_{tip} - v_{mouth})/v_{mouth}$, where $v_{tip} = \delta d_c/\delta t$ and $v_{mouth} = \delta w_c/\delta t$ are the speeds of crack deepening and opening, respectively. These variables describe the additional contribution of stresses during cracking and electrochemical corrosion, respectively. Fig 6 presents the evolutions of κ_v when F_x = 140–160/MPa; as shown, when κ_v exceeded 1 (or in the range of 1–2), a sharpened tip began to develop at the corrosion pit. Hence, the critical condition for the pit-to-crack transition can be identified as $\kappa_v > 1$. It is noteworthy that this condition is equivalent to the Tsujikawa–Kondo criterion [58, 59], i.e., the stress-induced crack propagation is faster than pitting because of corrosion. For the first time, we numerically confirmed this criterion and proposed a method to predict the lifetime of a structure based on this criterion. As κ_v ($\kappa_v > 2$) increased, the crack surface became wavy gradually (the blue and red lines at 40 and 60/min, respectively), which was observed in the experiments, as exemplified by crack "A" in the inset [60]. When κ_v increased further, e.g., when $\kappa_v > 15$ at the blue curve, the crack resembled a cylindrical (or rectangular in 2D) hole, similar to crack "B" in the inset [60].

Fig. 7

Fig 7 (a) shows the evolutions of the von Mises stress at the crack tip, σ_{mises}, when F_x = 140–160/MPa, where an upward but non-smooth trend is exhibited. After the initial rapid

increase in stress owing to the elastic deformation and pitting, the subsequent elastoplastic deformation (e.g., tip blunting) reduced the rate of stress increase. After 60/mins, the maximum equivalent stress was approximately 420/MPa for F_x = 160/MPa (the solid blue line in Fig. 7(a)), which might be similar to the ultimate tensile strength of some steels. As the metal was subjected to uniaxial tension, Mode-I crack occurred. Hence, the stress-intensity factor for Mode-I crack, K_I, was employed to evaluate the failure induced by SCC. K_I can be calculated based on the strain energy release rate as follows:

$$K_I = \sqrt{-\frac{E}{t_s}\partial\left(\int_\Omega \psi^{mech} dv\right)\Big/\partial d_c}\,, \tag{33}$$

where $t_s = l_{ref}$ is the thickness of the sample, and $-\partial\left(\int_\Omega \psi^{mech} dv\right)\Big/\left(t_s \partial d_c\right)$ is the strain energy release rate with an increase in the crack depth, d_c. The dashed curves in Fig. 7(a) show that K_I increases at a gradually increasing rate. Fig. 7(b) shows the variations in the crack propagation speed, denoted by v_{tip}, against K_I. As the vertical axis is on a logarithmic scale, the straight lines in Fig. 7(b) indicate exponential relations, which suggest that the effect of K_I on the speed of SCC is significant after it exceeds a critical value. As K_I increased, the crack propagation speed increased exponentially until fracture, which is consistent with the experimental observations [57, 61].

Fig. 8

Based on an experiment [57], stress affects the electrochemical environment within the crack. To quantify this effect, the evolution of the difference in the concentration of M^{n+} at the tip and mouth of the crack, i.e., $c_{M^{n+}}^{tip} - c_{M^{n+}}^{mouth}$, is shown in Fig. 8(a), where F_x = 140–160/MPa.

The gradual increase in the difference between $c_{M^{n+}}^{tip}$ and $c_{M^{n+}}^{mouth}$ was due to mechanical loading because (*i*) the diffusion path to the tip of crack was longer than that to the mouth, and (*ii*) the concentrated stress at the crack tip accelerated the metal dissolution. Furthermore, with the increase in F_x, the distribution of metallic ions became more heterogeneous, indicating a more localized corrosion induced by the local stress field. The local accumulation of positive charges of M^{n+} resulted in a heterogeneous distribution of electropotential within the crack, as shown in Fig. 8(b), wherein the electropotential difference between those at the tip and the mouth of the crack is shown. These numerical results are consistent with the experimental observation reported by MacDonald *et al.* [57].

Fig. 9

To separate the effects of stress and reaction kinetics and investigate their coupling effect on SCC, the evolutions of the pit/crack depth, d_c, for five scenarios are presented in Fig. 9. Scenario I involves all the couplings introduced above; in Scenario II, the enhanced stress effect on the reaction kinetics (i.e., Eq. (20)) are disregarded; Scenarios IV and V represent the cracks resulting from mere corrosion and stress only, respectively; Scenario III is a superposition of curves IV and V. In Scenarios IV and V, a semi-circular pit (due to the uniform reaction rate) and a wavy vertical crack (induced by stress) were observed, which resulted in depths of 16 and 15/μm at 60/min (the end of simulation), respectively. These two depths were much smaller than those due to coupling effects (I and II), indicating that neither stress nor electrochemical process alone can be the primary cause of SCC. Moreover, their superposition,

represented by curve III, was much lower than curves I and II involving MCC, demonstrating that the severe SCC was a result of the conjoint action of stress and the corrosive environment rather than their superposition. Comparing curves I and II, it is clear that if the stress term enhances corrosion kinetics by shifting the equilibrium potential to the left, as expressed in Eq. (20), then SCC will be further improved.

Fig. 10

A metallic component is typically subjected to various types of mechanical loading, resulting in SCC. A mechanical loading can be either a surface traction (F_x) or a surface displacement (u_x). Using the predefined simulation model, we compared the cases of F_x = 160/MPa and u_x = 0.08/μm, which initially resulted in similar far-field normal stresses. Fig. 10 shows the variations in crack depth with time for these two cases. Apparently, the surface traction resulted in an accelerated cracking, whereas the displacement boundary condition resulted in a stable crack growth, as clearly shown in the inset of Fig. 10, where the cracking speed v_{tip} is plotted against time. Such a difference is characteristic of fracture mechanics: if the sample is subjected to a displacement boundary condition, then the effect of crack morphology on stress distribution is finite, and cracking is a stable and slow process. This applies to SCC, as shown in Fig. 11(a), wherein the variations in the K_I can be compared. For the displacement boundary condition, K_I increased much slower. In Fig. 11(b), the contour plots of σ_{mises} are presented. As shown, the stress concentration area (e.g., the red and orange areas) did not increase with time when the displacement boundary condition was applied;

however, it expanded rapidly when traction was applied.

Fig. 11

Fig. 12

Finally, we examined the effect of the initial geometry on the crack growth. It is noteworthy that we set the initial pit to be a triangle with an initial depth of b = 7.5/μm. For other depths, such as b = 0, 2.5, and 5/μm, Fig. 12 (a) shows the evolutions of the pit/crack when the metallic component was subjected to the traction boundary condition, F_x = 160/MPa. As shown, for a smaller b, the early development of the pit was kinetically mediated, which resulted in a semi-circular shape as the reaction kinetics was independent of orientation. With the development of the pit, stresses became more concentrated at the tip, which ultimate resulted in SCC. The variation in the rate difference between SCC and mere corrosion, κ_v, was plotted, as shown in Fig 12(b). Similarly, it was indicated that the pit-to-crack transition occurred when $\kappa_v > 1$. Next, we plotted the critical depth of the pit that enabled the occurrence of the pit-to-crack transition, denoted by $d_c^{\text{pit-to-crack}}$, against b in the inset of Fig. 12(b). As shown, $d_c^{\text{pit-to-crack}}$ decreased with b at a reducing rate, which implies the high sensitivity of the SCC to the severity of the initial surface damage.

4. Conclusions

A new PF model was proposed to address the MCC in SCC. The interface migration associated with pitting and cracking was described using the Allen–Cahn-type equation, which

incorporates the theory of strain energy release rate in fracture mechanics, and the generalized BV relation describing an electrochemical reaction. Furthermore, Gutman's expressions were used to address the enhanced MCC, where stress affected the reaction rate or the equilibrium potential (see Eq. B1) during oxidation. Finally, a set of governing equations, including the Nernst–Planck–Poisson model for diffusion and stress equilibrium equations for mechanical deformation, was solved using a commercial FEM package. The numerical model used can be corroborated based on the experimental results and analytical solutions of homogenous corrosion. Subsequently, we investigated the 2D SCC process. The main findings are as follows:

(1) Based on the PF model, the autocatalytic effect resulting from the relationship between stress and corrosion was predicted. The effect resulted in the formation of a pit, initiation of a crack, and cracking at an accelerated rate. A parameter, κ_v, defined as $(v_{tip} - v_{mouth})/v_{mouth}$, was introduced to quantitatively analyze the additional contributions of stresses during cracking and electrochemical corrosion. Subsequently, the critical condition of pit-to-crack transition at $\kappa_v > 1$ was revealed, which, for the first time, confirmed the Tsujikawa–Kondo criterion [58, 59], i.e., when a pit-to-crack transition occurs, the stress-induced crack propagation should be faster than the pitting caused by corrosion. It was indicated that after the critical condition was fulfilled, an exponential relation between the cracking speed, v_{tip}, and the stress-intensity-factor for Mode-I crack, K_I, was obtained, which agreed well with the experimental observation [57]; this similarly demonstrated the validity of the proposed PF

model. Additionally, it was observed that an increase in the applied traction resulted in a more heterogeneous distribution of cation concentration and electropotential and a more localized corrosion, which were similarly observed in experiments [57].

(2) The comparison among different MCC scenarios indicated that the coupling effect resulted in a more significant SCC than the linear combination of mechanical cracking and corrosion. Nevertheless, the well-known difference between Dirichlet (displacement) and Neumann (force) boundary conditions associated with the stability of crack propagation remained valid, i.e., the SCC was more critical when a metallic component was subjected to external forces. In this case, the effect of the initial pit depth or surface damage was significant.

Acknowledgments

CL acknowledges the support from Guangdong Major Project of Basic and Applied Basic Research (2019B030302011), International Sci & Tech Cooperation Program of GuangDong Province (2019A050510022) and the support from Natural Science Basic Research Plan in Shaanxi Province of China (No. 2019JQ-123). HHR acknowledges the support of the General Research Fund of the Hong Kong Research Grants Council (Grant No.: 15213619, Account code: Q73H).

Author Contribution

CL and HHR conceptualized the study. CL conducted PF modeling, simulation, and drafted the manuscript; HHR edited and polished the manuscript.

Additional Information

Competing Interest: The authors declare no competing interests.

Data Availability

The data that support the findings of this study are available from the corresponding author upon reasonable request.

Appendix A

Considering that the forward and backward reactions take place simultaneously, the net reaction rate, expressed in the Arrhenius form, is:

$$r = k^0 \left(\exp\left(-\frac{\mu_{TS} - \mu_R}{RT} \right) - \exp\left(-\frac{\mu_{TS} - \mu_P}{RT} \right) \right), \quad \text{(A.1)}$$

where μ_R and μ_P are the chemical potentials of reactants and products, respectively; μ_{TS} is the chemical potential at the transition state. For a reaction involving multiple reactants and products, μ_R and μ_P can be expressed as:

$$\mu_R = RT \ln\left(\prod_i \left(a_{R_i^{X_i}} \right)^{n_i} \right) + \sum_i n_i \mu_{R_i^{X_i}}^{ex}, \quad \text{(A.2a)}$$

and $\mu_{\mathrm{P}} = RT\ln\left(\prod_{\mathrm{j}}\left(a_{\mathrm{P}_{\mathrm{j}}^{z_{\mathrm{j}}}}\right)^{n_{\mathrm{j}}}\right) + \sum_{\mathrm{j}} n_{\mathrm{j}}\mu_{\mathrm{P}_{\mathrm{j}}^{z_{\mathrm{j}}}}^{\mathrm{ex}}$, (A.2b)

where a_* and μ_*^{ex} are the activity and the excess chemical potential of $*$, respectively. According to the definition of Bazant [62], the activity is only concentration dependent, defined as:

$$a_* = \exp\left(\frac{1}{RT}\left(\frac{\delta\left(\int_\Omega\left(\psi^{\mathrm{chem}}\right)d\omega\right)}{\delta c_*} - \mu_*^0\right)\right). \quad \text{(A.3a)}$$

Correspondingly, the excess chemical potential, μ_*^{ex}, is:

$$\mu_*^{\mathrm{ex}} = \frac{\delta\left(\int_\Omega \psi - \psi^{\mathrm{chem}} d\omega\right)}{\delta c_*} + \mu_*^0, \quad \text{(A.3b)}$$

which involves the contributions of mechanical energy, electric potential, and standard chemical potential. The chemical potential at the transition state, μ_{TS}, is defined as [62]:

$$\mu_{\mathrm{TS}} = RT\ln a^{\mathrm{TS}} + \rho\sum_{\mathrm{i}} n_{\mathrm{i}}\mu_{\mathrm{R}_{\mathrm{i}}^{X_{\mathrm{i}}}}^{\mathrm{ex}} + (1-\rho)\sum_{\mathrm{j}} n_{\mathrm{j}}\mu_{\mathrm{P}_{\mathrm{j}}^{z_{\mathrm{j}}}}^{\mathrm{ex}}, \quad \text{(A.4)}$$

Substituting Eqs. (A.2a), (A.2b) and (A.4) into Eq. (A.1), the reaction rate, r, can be finally derived in the form of Eq. (16).

Appendix B

If we set reaction rate r = 0, the electric potential difference at the electrode-electrolyte interface under an electrochemical equilibrium can be derived as:

$$\Delta\varphi_{\mathrm{eq}} = \left(\varphi_{\mathrm{S}} - \varphi_{\mathrm{L}}\right)_{\mathrm{eq}} = \frac{1}{nF}\left(\begin{array}{l} RT\ln\left(\frac{a_{\mathrm{P}}}{a_{\mathrm{R}}}\right) + \mu_{\mathrm{M}^{n+}}^0 - \frac{V_{\mathrm{M}}}{3}\left|tr\left(\boldsymbol{\sigma}\right)\right| - RT\ln\left(\frac{\upsilon\alpha\varepsilon_{\mathrm{eq}}^{\mathrm{p}}}{N_0}+1\right) \\ -\frac{\partial p(\phi)}{c_{\mathrm{M}}^{\mathrm{ref}}\partial\phi}\left(\frac{1}{2}\left(\boldsymbol{\varepsilon}^{\mathrm{e}}\right)^T\cdot\left(\mathbf{D}^{\mathrm{e}}\boldsymbol{\varepsilon}^{\mathrm{e}}\right) + \left(\sigma_{\mathrm{y}} + \frac{1}{2}H\varepsilon_{\mathrm{eq}}^{\mathrm{p}}\right)\varepsilon_{\mathrm{eq}}^{\mathrm{p}}\right) \end{array}\right). \quad \text{(B.1)}$$

The reaction takes place under the overpotential, η, defined as $\eta = \Delta\varphi - \Delta\varphi_{eq}$. Substituting overpotential η into Eq. (16) leads to the generalized BV equation, expressed as:

$$r = \frac{k^0}{a_{TS}} \left(a_R\right)^{\rho} \left(a_P\right)^{(1-\rho)} \left(\exp\left(\frac{(1-\rho) nF\eta}{RT} \right) - \exp\left(-\frac{\rho nF\eta}{RT} \right) \right). \quad \text{(B.2)}$$

Appendix C

Omitting the effect of concentration and stress, the reference chemical potential, $\mu^0_{M^{n+}}$, can be expressed as $\mu^0_{M^{n+}} = nF\Delta\varphi_{eq}$ (based on Eq. (B.1)), where n and F are listed in table 1 and the equilibrium electric potential, $\Delta\varphi_{eq}$, is about -0.6/V [63]. Thus, the reference chemical potential, $\mu^0_{M^{n+}}$ can be determined to be about -100 kJ mol^{-1}.

Following Caginalp [64], 1D analytical solutions for the velocity of phase boundary migration can be obtained from Eq. (28) under the steady state conditions (i.e., the concentration, electric potential, and displacement field remaining unvaried) expressed as:

$$v = M_\phi l \left(\frac{1}{2} \left(\boldsymbol{\varepsilon}^e\right)^T \cdot \left(\mathbf{D}^e \boldsymbol{\varepsilon}^e\right) + \left(\sigma_y + \frac{1}{2} H \varepsilon^p_{eq} \right) \varepsilon^p_{eq} \right) + L^{bulk} l \left(a_R \exp\left(\frac{(1-\rho)\left(\mu^{ex}_R - \mu^{ex}_P\right)}{RT} \right) - \bar{c}_{M^{n+}} \exp\left(-\frac{\rho\left(\mu^{ex}_R - \mu^{ex}_P\right)}{RT} \right) \right), \quad \text{(C.1)}$$

where v is the velocity of phase boundary migration.

If the mechanical loading is not applied, the effects of stress and the fracture energy are negligible, which leads to a 1D velocity of phase migration due to corrosion, given by:

$$v = L^{\text{bulk}} l \left(\begin{array}{l} \exp\left(\dfrac{(1-\rho)\left(nF\left(\varphi_S - \varphi_L\right) - \mu^0_{M^{n+}}\right)}{RT} \right) - \\ \bar{c}_{M^{n+}} \exp\left(- \dfrac{\rho n F \left(nF\left(\varphi_S - \varphi_L\right) - \mu^0_{M^{n+}}\right)}{RT} \right) \end{array} \right). \quad \text{(C.2)}$$

Letting $v = 0$, a critical concentration, $\bar{c}^{cr}_{M^{n+}}$, can be estimated from Eq. (C.2):

$$\bar{c}^{cr}_{M^{n+}} = \exp\left(\frac{nF\left(\varphi_S - \varphi_L\right) - \mu^0_{M^{n+}}}{RT} \right). \quad \text{(C.3)}$$

It means that if the local concentration is larger than this critical value, the corrosion would be stopped, which results in a diffusion-controlled corrosion process. Hence, the increase in the applied potential leads to the more kinetics-mediated corrosion because the critical M^{n+} concentration is more difficult to achieve. Correspondingly, the higher diffusivity of M^{n+} in electrolyte reduces the accumulation of M^{n+} at the metal surface, resulting in the kinetics-mediated corrosion behavior.

Eq. (C.2) can be recast as:

$$v = L^{\text{bulk}} l \exp\left(\frac{(1-\rho)\left(nF\left(\varphi_S - \varphi_L\right) - \mu^0_{M^{n+}}\right)}{RT} \right). \quad \text{(C.4)}$$

With Eq. (C.4), if the applied potentials, φ_s and φ_L, and the rate of homogenous corrosion, v, are known, the kinetic coefficient, L^{bulk}, can be estimated. Based on the experimental results provided in [52], wherein the applied potential in metallic electrode and electrolyte are -250/mV and 0/mV, respectively, the corrosion rate can be 11.6/mm year^{-1}. Thus, the kinetic coefficient, L^{bulk}, is determined to be 1.5×10^{-7}/s^{-1} with l = 2.5/μm, ρ = 0.5, φ_s = -250/mV, φ_L = 0/mV, n = 2 and $\mu^0_{M^{n+}}$ = -100/kJ mol^{-1}.

Fig. C.1

Reference

[1] B. Hou, X. Li, X. Ma, C. Du, D. Zhang, M. Zheng, W. Xu, D. Lu, F. Ma, The cost of corrosion in China, Npj Mater. Degrad. 1 (2017) 4.

[2] C.A. Loto, Stress corrosion cracking: characteristics, mechanisms and experimental study, Int J Adv. Manuf. Technol. 93 (2017) 3567–3582.

[3] E.G. Coleman, D.C. Weinstein, W. Rostoker, On a surface energy mechanism for stress-corrosion cracking, Acta Metall. 9 (1961) 491– 496.

[4] S.P. Lynch, Environmentally assisted cracking: overview of evidence for an adsorption-induced localized-slip process, Acta Metall. 36 (1988) 2639–2661.

[5] J.C. Scully, Stress corrosion crack propagation: A constant charge criterion. Corros. Sci. 15 (1975) 207–224.

[6] J.C. Scully, The interaction of strain-rate and repassivation rate in stress corrosion crack propagation. Corros. Sci. 20 (1980) 997–1016.

[7] F.P. Ford, Quantitative prediction of environmentally assisted cracking, Corrosion 52 (1996) 375–395.

[8] R.H. Jones, Analysis of hydrogen-induced subcritical intergranular crack growth of iron and nickel, Acta Mater. 38 (1990) 1703–1718.

[9] H.K. Birnbaum, P. Sofronis, Hydrogen-enhanced localized plasticity-a mechanism for hydrogen-related fracture, Mater. Sci. Eng. A 176 (1994) 191–202.

[10] D. Delafosse, T. Magnin, Hydrogen induced plasticity in stress corrosion cracking of engineering systems, Eng. Fract. Mech. 68 (2001) 693–729.

[11] M.G. Fontana, N.D. Greene, Corrosion engineering, 2nd edn. McGraw-Hill Int. Ed., p 91.

[12] S.S. Singh, T.J. Stannard, X. Xiao, N. Chawla, In situ X-ray microtomography of stress corrosion cracking and corrosion fatigue in aluminum alloys, JOM 69 (2017) 1404–1414

[13] R. Schoell, L. Xi, Y.C. Zhao, X. Wu, Z.Z. Yu, P. Kenesei, J. Almer, Z. Shayer, D. Kaoumi, In situ synchrotron X-ray tomography of 304 stainless steels undergoing chlorine-induced stress corrosion cracking, Corros. Sci. 170 (2020) 108687.

[14] J. Zhang, S. Kalnaus, M. Behrooz, Y. Jiang, Effect of loading history on stress corrosion cracking of 7075-T651 aluminum alloy in saline aqueous environment, Metall. Mater. Trans. A 42 (2011) 448–460.

[15] K. Van Minnebruggen, S. Hertelé, M.A. Verstraete, W. De Waele, Crack growth characterization in single-edge notched tension testing by means of direct current potential drop measurement, Int. J. Press. Vessel. Pip. 156 (2017) 68–78.

[16] D.D. MacDonald, M. Urquidi-MacDonald, A coupled environment model for stress corrosion cracking in sensitized type 304 stainless steel in LWR environments, Corros. Sci. 32 (1991) 51–81.

[17] R.C. Newman, Developments in the slip-dissolution model of stress corrosion cracking, Corrosion 50 (1994) 682–686.

[18] A. Turnbull, L. Wright, L. Crocker, New insight into the pit-to-crack transition from finite

element analysis of the stress and strain distribution around a corrosion pit, Corros. Sci. 52 (2010) 1492–1498.

[19] L.K. Zhu, Y. Yan, L.J. Qiao, A.A. Volinsky, Stainless steel pitting and early-stage stress corrosion cracking under ultra-low elastic load, Corros. Sci. 77 (2013)

[20] G. Meric de Bellefon, J.C. van Duysen, Finite element analysis of the influence of elastic anisotropy on stress intensification at stress corrosion cracking initiation sites in fcc alloys, J Nucl. Mater. 503 (2018) 22–29.

[21] I. Benedetti, V. Gulizzi, A. Milazzo, Grain-boundary modelling of hydrogen assisted intergranular stress corrosion cracking, Mech. Mater. 117 (2018) 137–151.

[22] P.T. Brewick, V.G. DeGiorgi, A.B. Geltmacher, S.M. Qidwai, Modeling the influence of microstructure on the stress distributions of corrosion pits, Corros. Sci. 158 (2019) 108111.

[23] P. Brewick, N. Kota, A. Lewis, V. DeGiorgi, A. Geltmacher, S. Qidwai, Microstructure-sensitive modeling of pitting corrosion: effect of the crystallographic orientation, Corros. Sci. 129 (2017) 54–69.

[24] A.S. Vagbharathi, S. Gopalakrishnan, An extended finite-element model coupled with level set method for analysis of growth of corrosion pits in metallic structures, Proc. R. Soc. A: Math. Phys. Eng. Sci. 470 (2014) 20140001.

[25] R. Duddu, Numerical modeling of corrosion pit propagation using the combined extended finite element and level set method, Comput. Mech. 54 (2014) 613–627.

[26] S. Scheiner, C. Hellmich, Stable pitting corrosion of stainless steel as diffusion controlled

dissolution process with a sharp moving electrode boundary, Corros. Sci., 49 (2007) 319–346.

[27] D. di Caprio, J. Stafiej, G. Lucianoc, L. Arurault, 3D cellular automata simulations of intra and intergranular corrosion, Corros. Sci. 112 (2016) 438–450.

[28] O.O. Fatoba, R. Leiva-Garcia, S.V. Lishchuk, N.O. Larrosa, R. Akid, Simulation of stress-assisted localized corrosion using a cellular automaton finite element approach, Corros. Sci. 137 (2018) 83–97.

[29] C. Chuanjie, M. Rujin, C. Airong, P. Zichao, T. Hao, Experimental study and 3D cellular automata simulation of corrosion pits on Q345 steel surface under salt-spray environment, Corros Sci 154 (2019) 80–89.

[30] Z. Chen, F. Bobaru, Peridynamic modeling of pitting corrosion damage, J. Mech. Phys. Solids 78 (2015) 352–381.

[31] S. Jafarzadeh, Z. Chen, S. Li, F. Bobaru, A peridynamic mechano-chemical damage model for stress-assisted corrosion, Electrochim. Acta 323 (2019) 134795.

[32] Z. Chen, S. Jafarzadeh, J. Zhao, F. Bobaru, A coupled mechano-chemical peridynamic model for pit-to-crack transition in stress-corrosion cracking, J Mech. Phys. Solids 146 (2021) 104203.

[33] P. Ståhle, E. Hansen, Phase field modelling of stress corrosion, Eng. Fail. Anal. 47 (2015) 241–251.

[34] W. Mai, S. Soghrati, A phase field model for simulating the stress corrosion cracking

initiated from pits, Corros. Sci. 125 (2017) 87–98.

[35] T.T. Nguyen, J. Bolivar, J. Réthoré, M.C. Baietto, M. Fregonese, A phase field method for modeling stress corrosion crack propagation in a nickel base alloy, Int. J. Solids Struct. 112 (2017) 65–82.

[36] T.T. Nguyen, J. Réthoré, M.C. Baietto, J. Bolivar, M. Fregonese, S.P. Bordas, Modeling of inter- and transgranular stress corrosion crack propagation in polycrystalline material by using phase field method, J. Mech. Behav. Mater. 26 (2017) 181–191.

[37] T.T. Nguyen, J. Bolivar, Y. Shi, J. Réthoré, A. King, M. Fregonese, J. Adrien, J.Y. Buffiere, M.C. Baietto, A phase field method for modeling anodic dissolution induced stress corrosion crack propagation, Corros. Sci. 132 (2018) 146–160.

[38] C. Lin, H.H. Ruan, S.Q. Shi, Phase field study of mechanico-electrochemical corrosion, Electrochim. Acta 310 (2019) 240–255.

[39] C. Lin, H.H. Ruan, Multi-phase-field modeling of localized corrosion involving galvanic pitting and mechano-electrochemical coupling, Corros. Sci. 177 (2020) 108900.

[40] R.K. Ren, S. Zhang, X.L. Pang, K.W. Gao, A novel observation of the interaction between the macroelastic stress and electrochemical corrosion of low carbon steel in 3.5 wt% NaCl solution, Electrochim. Acta 85 (2012) 283–294.

[41] X.H. Wang, X.H. Tang, L.W. Wang, C. Wang, Z.Z. Guo, Corrosion behavior of X80 pipeline steel under coupling effect of stress and stray current, Int. J. Electrochem. Sci. 9 (2014) 4574–4588.

[42] H.Q. Yang, Q. Zhang, S.S. Tu, Y. Wang, Y.M. Li, Y. Huang, Effects of inhomogeneous elastic stress on corrosion behaviour of Q235 steel in 3.5% NaCl solution using a novel multi-channel electrode technique, Corros. Sci. 110 (2016) 1–14.

[43] M. Cerit, K. Genel, S. Eksi, Numerical investigation on stress concentration of corrosion pit, Eng. Fail. Anal., 16 (2009) 2467–2472.

[44] X. Feng, X. Lu, Y. Zuo, N. Zhuang, D. Chen, The Effect of Deformation on Metastable Pitting of 304 Stainless Steel Chloride Contaminated Concrete Pore Solution, Corros. Sci., 103 (2015) 223–229.

[45] S.-L. Wang, R. F. Sekerka, A. A. Wheeler, B. T. Murray, S. R. Coriell, R. J. Braun, G. B. McFadden, Thermodynamically-consistent phase-field models for solidification, Physica D, 69, 189–200 (1993)

[46] P. J. Loew, B. Peters, L.A.A. Beex, Rate-dependent phase-field damage modeling of rubber and its experimental parameter identification, J Mech. Phys. Solids 127 (2019) 266–294.

[47] T.-T. Nguyen, J. Yvonnet, M. Bornert, C. Chateau, K. Sab, R. Romani, R.L. Roy, On the choice of parameters in the phase field method for simulating crack initiation with experimental validation, Int. J. Fract. 197 (2016) 213–226.

[48] A.M. Kuznetsov, J. Ulstrup, Electron Transfer in Chemistry and Biology: An Introduction to the Theory, Wiley: Chichester, U.K. (1999).

[49] E.M. Gutman, Mechanochemistry of solid surfaces, World Scientific, 1994.

[50] L.Y. Xu, Y.F. Cheng, Corrosion of X100 pipeline steel under plastic strain in a neutral pH bicarbonate solution, Corros. Sci. 64 (2012) 145–152.

[51] L. Onsager, S. Machlup, Fluctuations and irreversible processes, Phys. Rev. 91(1953) 1505.

[52] R. W. Revie, & H. H. Uhlig, Uhlig's corrosion handbook. 3rd edn, Wiley, 2011.

[53] COMSOL Multiphysics Users' Guide. Available from: http://www.comsol.com/.

[54] D. A. Cogswell, Toward Quantitative Phase-field Modeling of Dendritic Electrodeposition, Phys. Rev. E 92 (2015) 011301(R).

[55] P. Ernst, R.C. Newman, Pit growth studies in stainless steel foils. I. Introduction and pit growth kinetics. Corros. Sci. 44 (2002) 927–941.

[56] S. Scheiner, C. Hellmich, Stable pitting corrosion of stainless steel as diffusion-controlled dissolution process with a sharp moving electrode boundary. Corros. Sci. 49 (2007) 319–346.

[57] D.D. MacDonald, M. Urquidi-MacDonald, A coupled environment model for stress corrosion cracking in sensitized type 304 stainless steel in LWR environments, Corros. Sci. 32 (1991) 51–81.

[58] Y. Kondo, Prediction of fatigue crack initiation life based on pit growth, Corrosion 45 (1989) 7–11.

[59] S. Tsujikawa, Roles of localized corrosion on initiation of stress corrosion cracks for austenitic stainless steels in chloride environment, Stainless Steels’91 1 (1991) 48–55.

[60] H. Dai, S. Shi, C. Guo, X. Chen, Pits formation and stress corrosion cracking behavior of Q345R in hydrofluoric acid. Corros. Sci. 166 (2020) 108443.

[61] F.P. Ford, Quantitative prediction of environmentally assisted cracking, Corrosion 52 (1996) 375–395.

[62] M. Z. Bazant, Theory of chemical kinetics and charge transfer based on nonequilibrium thermodynamics, Acc. Chem. Res., 46, 1144–1160 (2013).

[63] M. Randall, M. Frandsen, The standard electrode potential of iron and the activity coefficient of ferrous chloride, J. Am. Chem. Soc. 54 (1932) 47–54.

[64] G. Caginalp, Stefan and hele-shaw type models as asymptotic limits of the phase-field equation, Phys. Rev.A 39 (1989) 5887–96.

Figure captions

Fig. 1 Schematics of SCC.

Fig. 2 (a) The geometry and boundary conditions of the simulation domain and (b) FE mesh used in simulation.

Fig. 3 The variation of corrosion rate v_c with the applied electrode potential φ_M resulting from a 1D simulation of homogeneous corrosion.

Fig. 4 (a) The increase in the pit depth, d_c, with time; (b) the variation of d_c at 100/mins against D_a; the evolutions of (c) concentrations, $c_{M^{n+}}$ and c_{Cl^-}, and (d) potential, φ_L, in the electrolyte near the tip of pit, for different Damkohler number, D_a, in the range of 0.27 – 2.7.

Fig. 5 (a) Evolution of inhomogeneous distribution of stress as a sharp vertical crack development and (b) the evolutions of the crack depth normal to the tip of crack, d_c, and the crack width normal to the mouth of crack, w_c.

Fig. 6 Evolution of the variable, κ_v, with time for the metallic electrode subjected to different tractions (F_x = 140/MPa – 160/MPa). κ_v is defined as $\kappa_v = (v_{tip} - v_{mouth})/v_{mouth}$, which characterizes the rate difference between SCC and mere corrosion.

Fig. 7 (a) evolutions of von Mises stress at the tip of the crack, σ_{mises}, and the stress-intensity-factor for Mode-I crack, K_I, and (b) variations of cracking velocity, denoted by v_{tip}, with K_I when F_x = 140 – 160/MPa.

Fig. 8 Evolutions of (a) the concentration (M^{n+}) and (b) electropotential differences at the tip and mouth of crack, denoted by $c_{M^{n+}}^{tip} - c_{M^{n+}}^{mouth}$ and $\varphi^{tip} - \varphi^{mouth}$, respectively, when F_x = 140 – 160/MPa.

Fig. 9 Evolutions of crack depth, d_c, with time for the sample subjected to the traction, F_x =160/MPa. Herein, curves I, IV and V represent respectively the scenarios that the crack results from the MCC, mere corrosion, and stress only. Curve III is a simple superposition of lines IV and V, and curve II represents the scenario that the enhanced stress effect on reaction kinetics (i.e., Eq. (20)) are ignored.

Fig. 10 The difference between traction (F_x = 160/MPa) and displacement (u_x = 0.08/μm) boundary conditions in terms of the variation of crack depth, d_c, with time.

Fig. 11 (a) Evolution of mises stress at the tip of crack, σ_{mises}, and the stress-intensity-factor for Mode-I crack, K_I, and (b) the corresponding contour plot of mises stress, when the sample is subjected to taction and displacement.

Fig. 12 (a) The contour plot of crack and (b) the evolution of variable, κ_v, with time for the samples subjected to the traction, F_x = 160/MPa, having the different initial pit, a = 7.5/μm and b = 0 – 7.5/μm.

Fig. C.1 Example of convergence curve for a simulation with the applied electrode potential, φ_M = -0.1/V, the kinetics coefficient, L^{bulk} = $1.5\times10^{-7}/s^{-1}$, and uniaxial traction, F_x = 140/MPa.

1 **Table**

	Parameter	Value
Reference length	l_{ref}	2.5/μm
Reference time	t_{ref}	60/s
Interfacial mobility	M_{ϕ}	1.5×10^{-4}/m^3 J^{-1} s^{-1} [37]
Fracture energy density	g_c	120/J m^{-2} [37]
Interface thickness	l	2.5/μm [37]
Young's modulus of the metal	E	200/GPa
Poisson's ratio of the metal	v	0.33
Initial yield strength of metal	σ_y^0	320/MPa
Linear strengthening modulus of metal	H	5/GPa
Reference concentration of metal	c_M^{ref}	1.4×10^{2}/mol L^{-1} [38]
Reference concentration of metal ion in electrolyte	$c_{M^{n+}}^{ref}$	5.436/mol L^{-1} [38]
Reference chemical potential of M^{n+}	$\mu_{M^{n+}}^0$	-100/kJ mol^{-1} (See Ref. [39] or Appendix D)
Coefficients to scale the contributions of corrosion kinetics to phase migration	L^{bulk}	1.5×10^{-7}/s^{-1} (See Appendix D)
Asymmetry factor	ρ	0.5 [38]

Diffusion coefficient in electrolyte	D^L	1×10^{-9}/m^2 s^{-1} [38]
Electric conductivity of electrolyte	ε^L	1/S m^{-1} [38]
Electric conductivity of metal	ε^S	10^7/S m^{-1} [38]
Ideal gas constant	R	8.314/J mol^{-1} K^{-1}
charge number of metallic ion M^{n+}	n	2
Faraday's constant	F	96485/C mol^{-1}
Coefficient to scale the effect of plasticity to electropotential	α	1.67×10^{11}/cm^2 [50]
Orientation-dependent factor	υ	0.45 [50]
Initial dislocation density	N_0	10^8/cm^2 [50]

Table 1 Parameters used in simulation

Dear Editors:

We are grateful for the comments and have thoroughly revise and improve the manuscript according to your suggestion. The revised manuscript with modification marks (highlighted in yellow background) is now submitted for your further consideration. In the separate response letter, your comments have been responded item-by-item and the corresponding changes in the manuscript were indicated with the page and line numbers.

Thank you and best regards.

Yours sincerely,

Prof. Haihui Ruan

Corresponding author:

Haihui Ruan, Tel.: + 852 2766 6648, Fax: +852 2365 4703, E-mail address: haihui.ruan@polyu.edu.hk

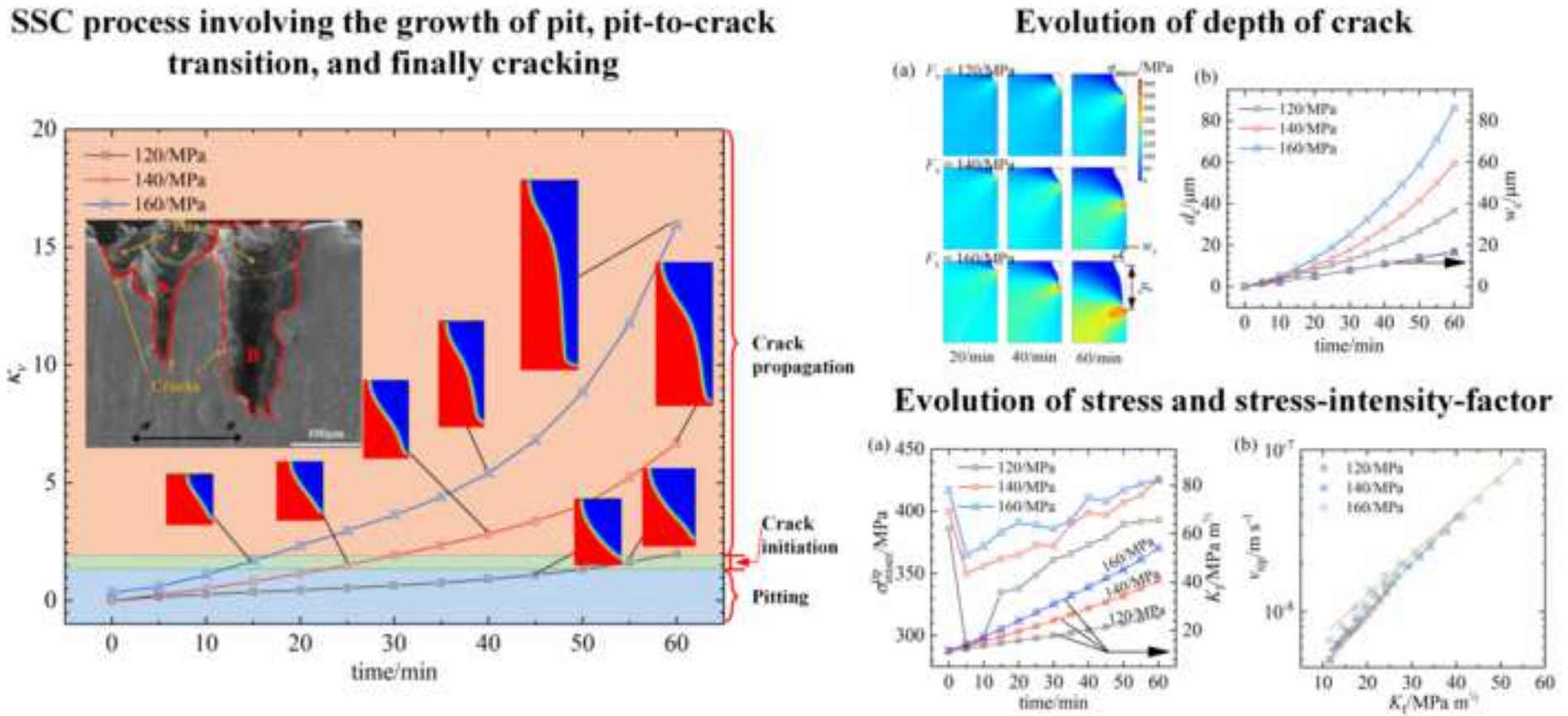

Figure 01

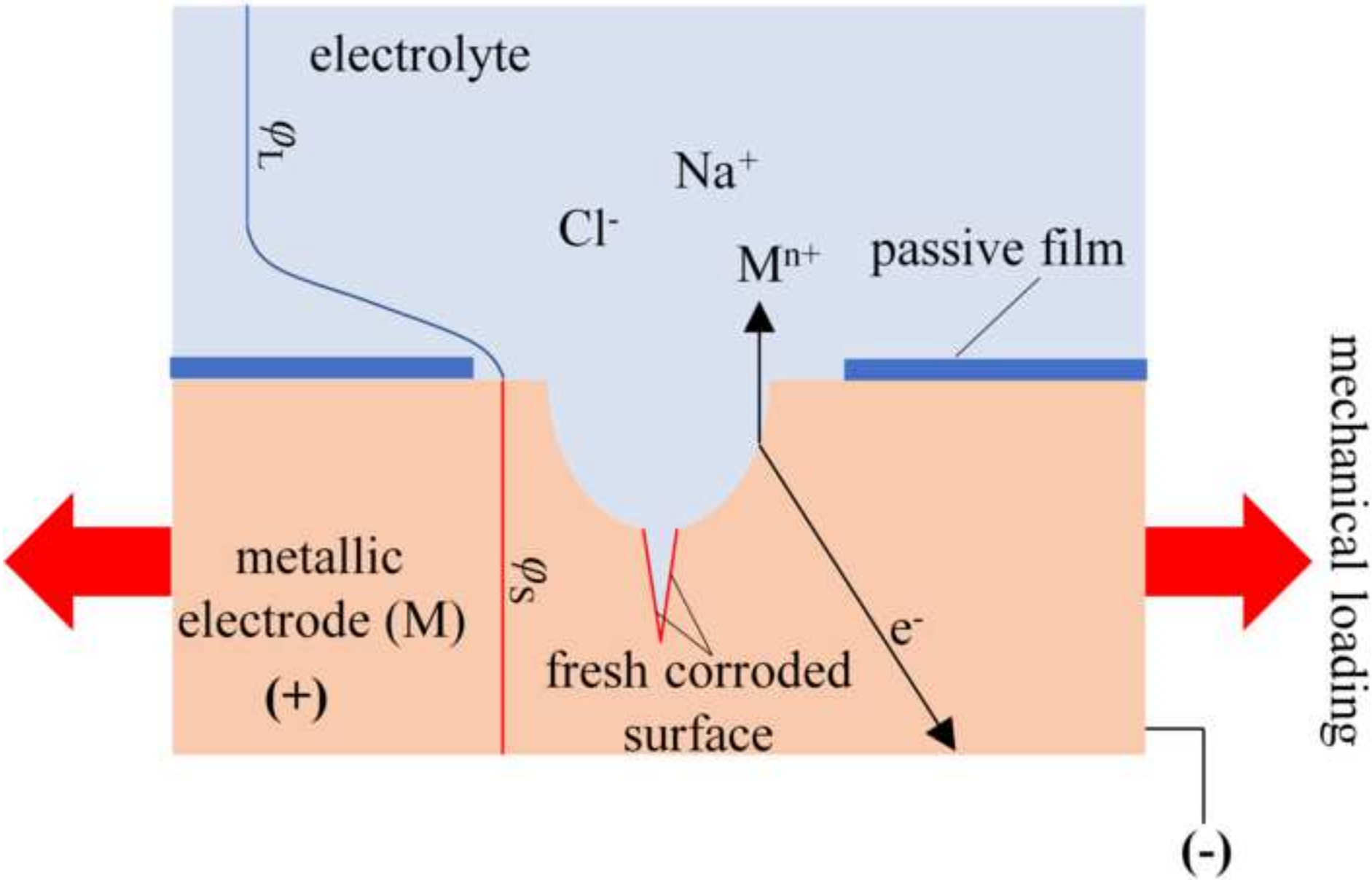

Figure 02

Click here to access/download;Figure(s);fig. 02.tif

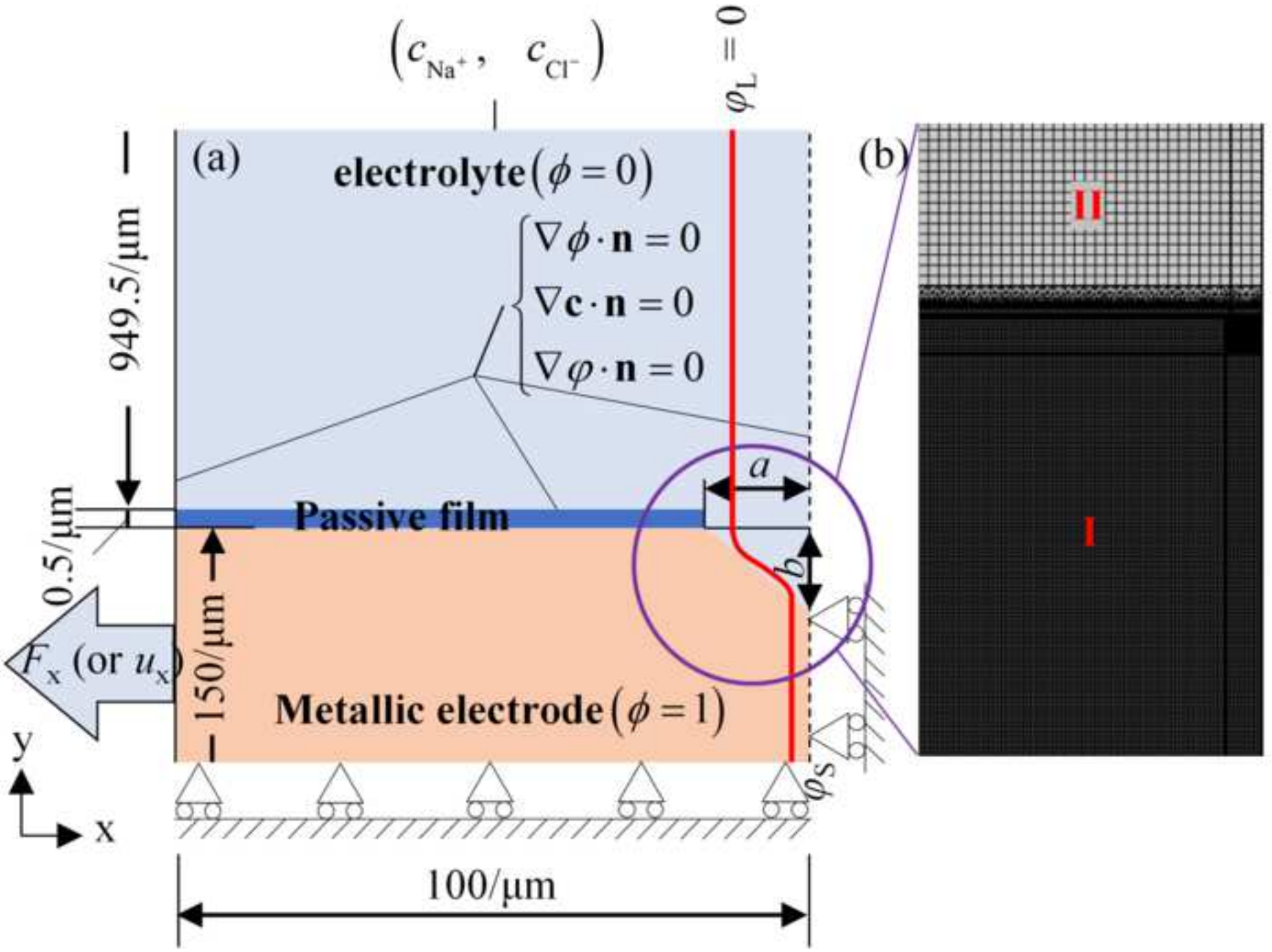

Figure 03

Click here to access/download;Figure(s);fig. 03.tif

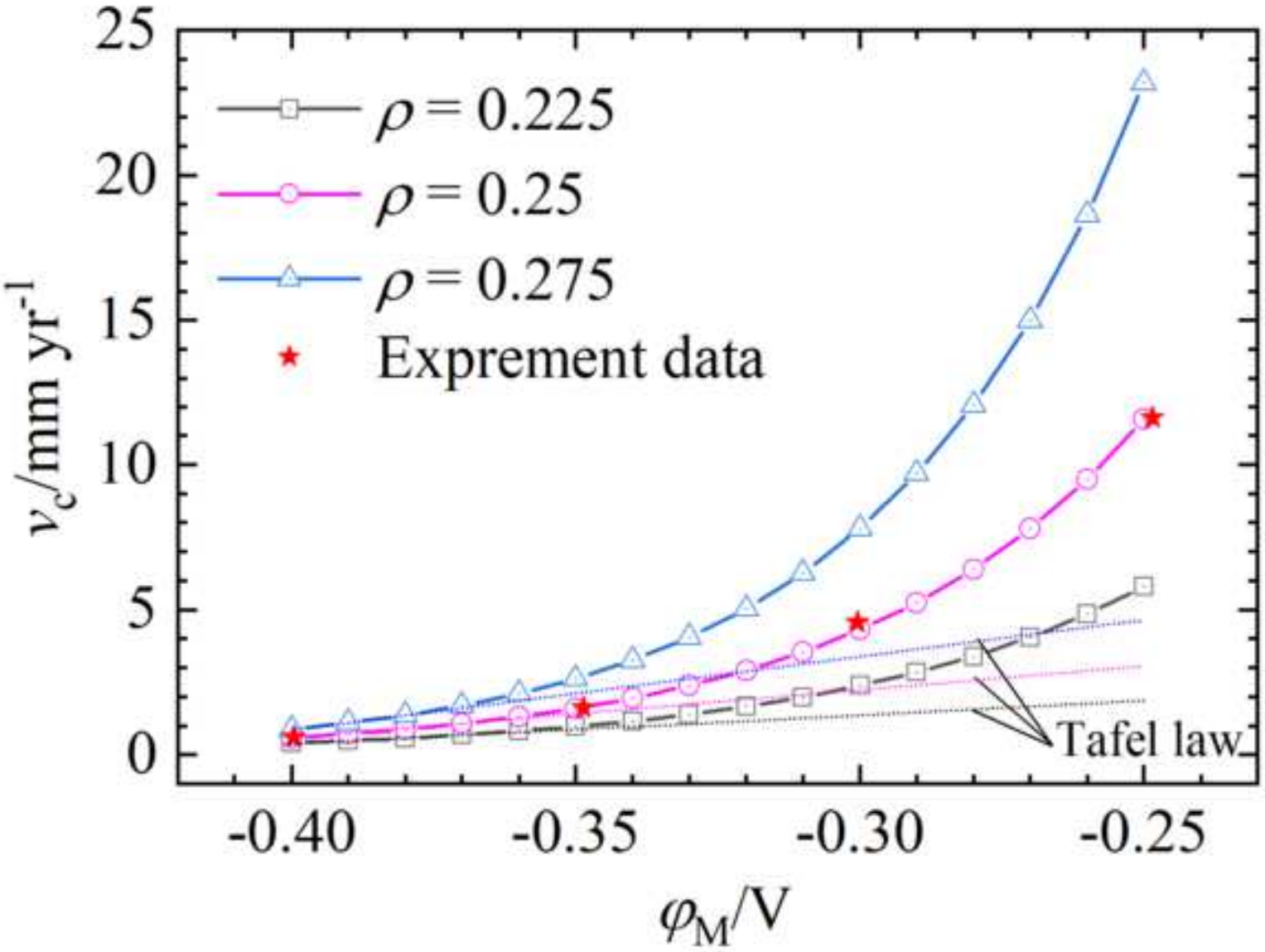

Figure 04

Click here to access/download;Figure(s);fig. 04.tif

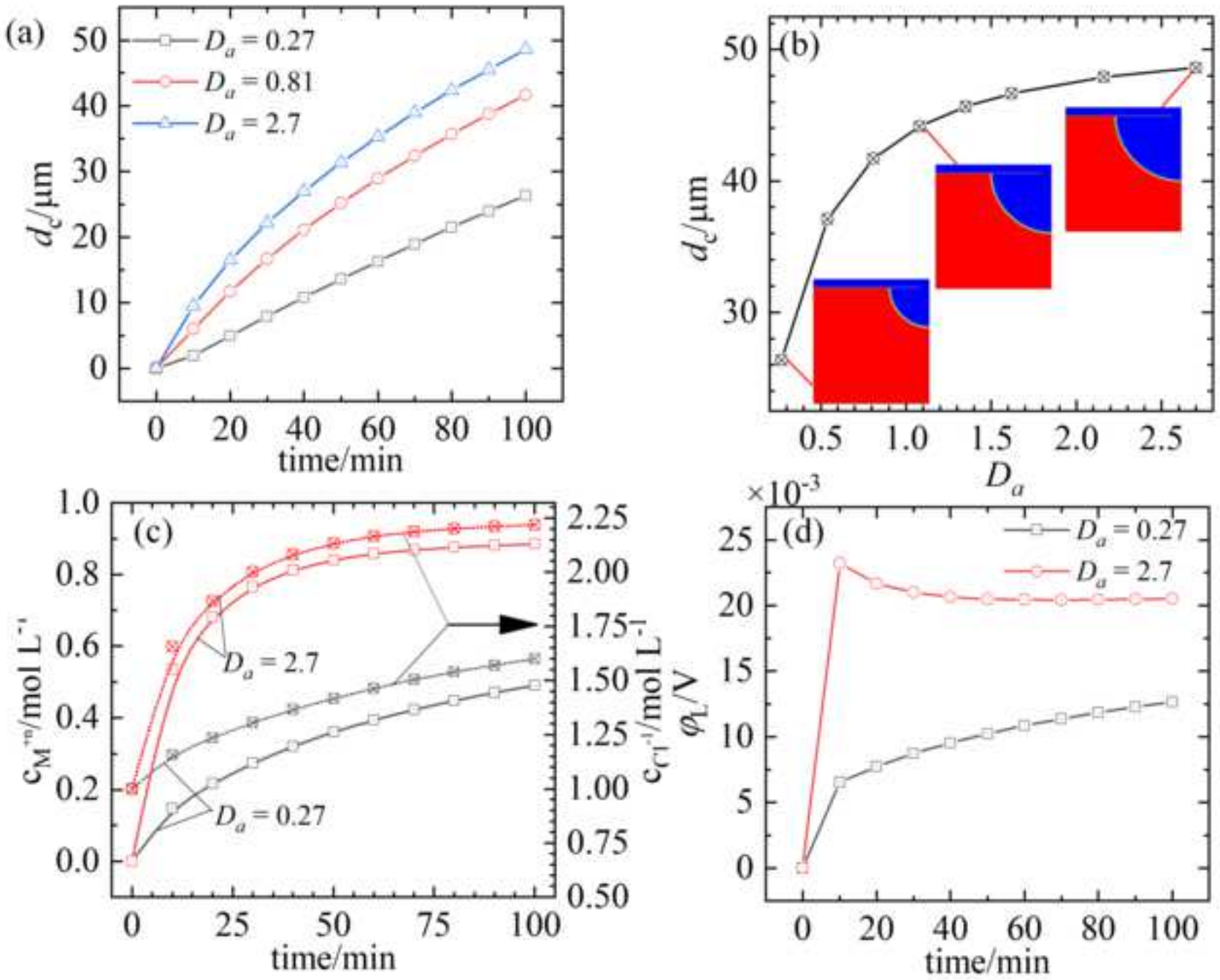

Figure 05

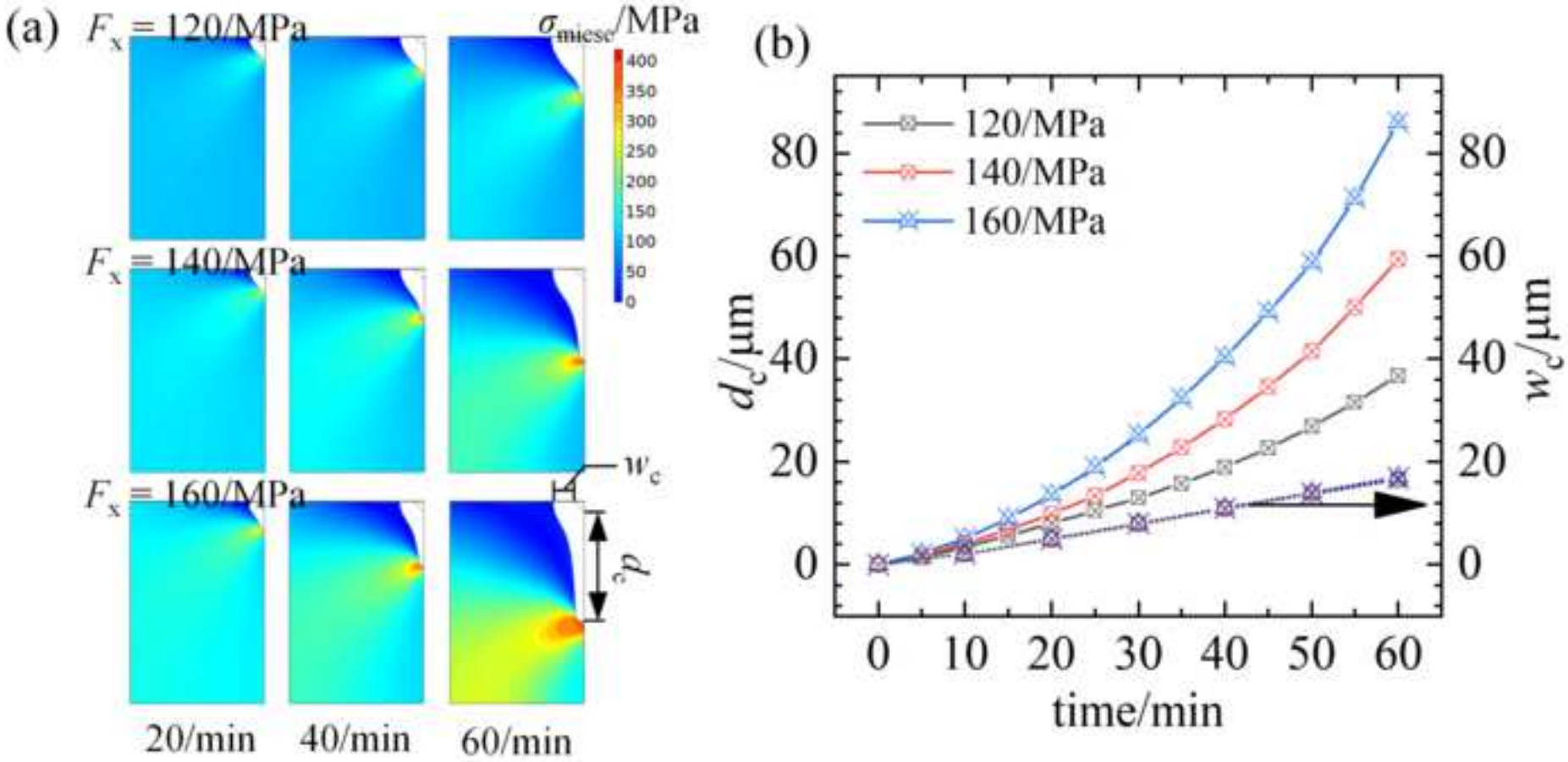

Figure 06

Click here to access/download;Figure(s);fig. 06.tif

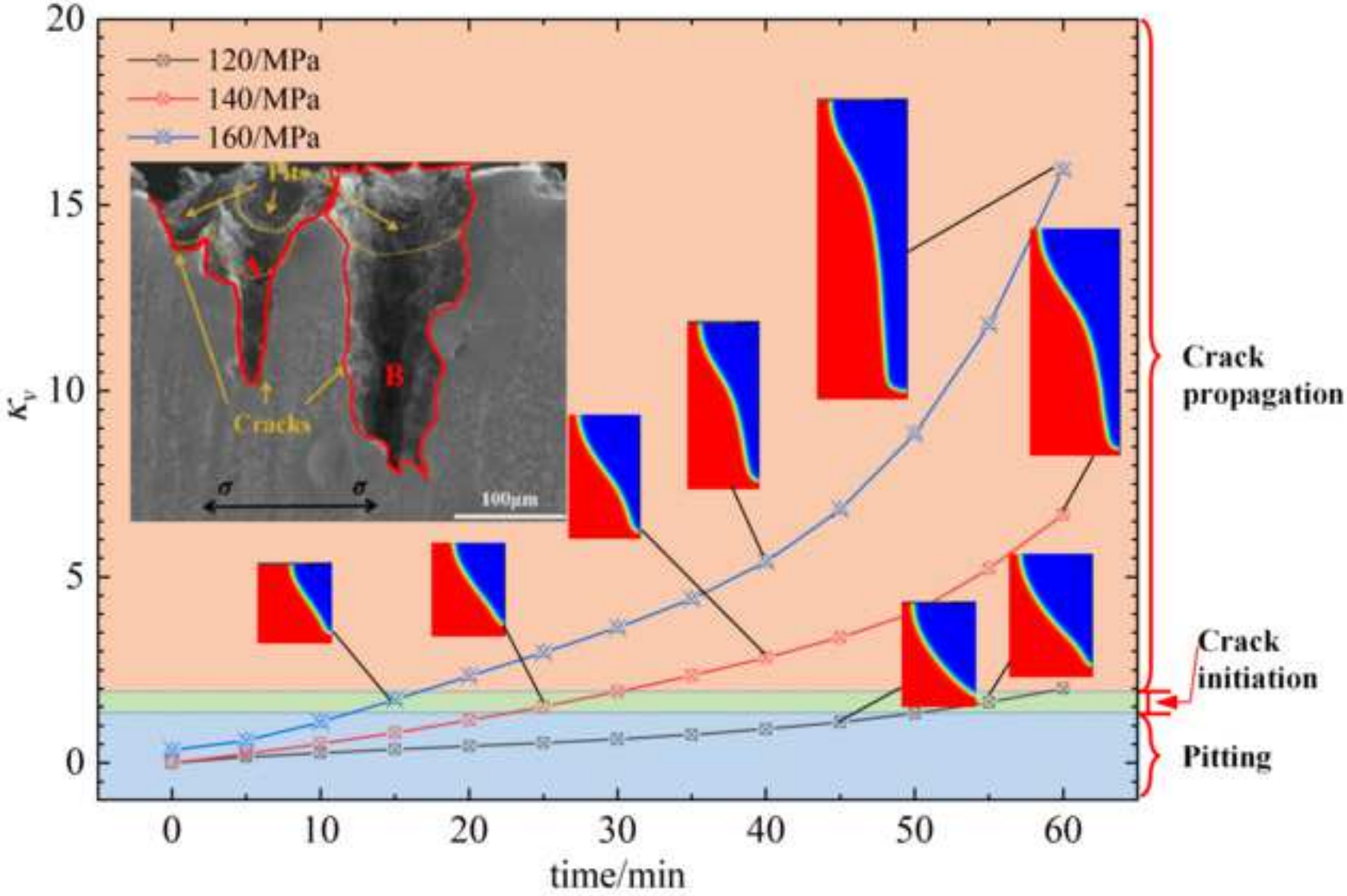

Figure 07

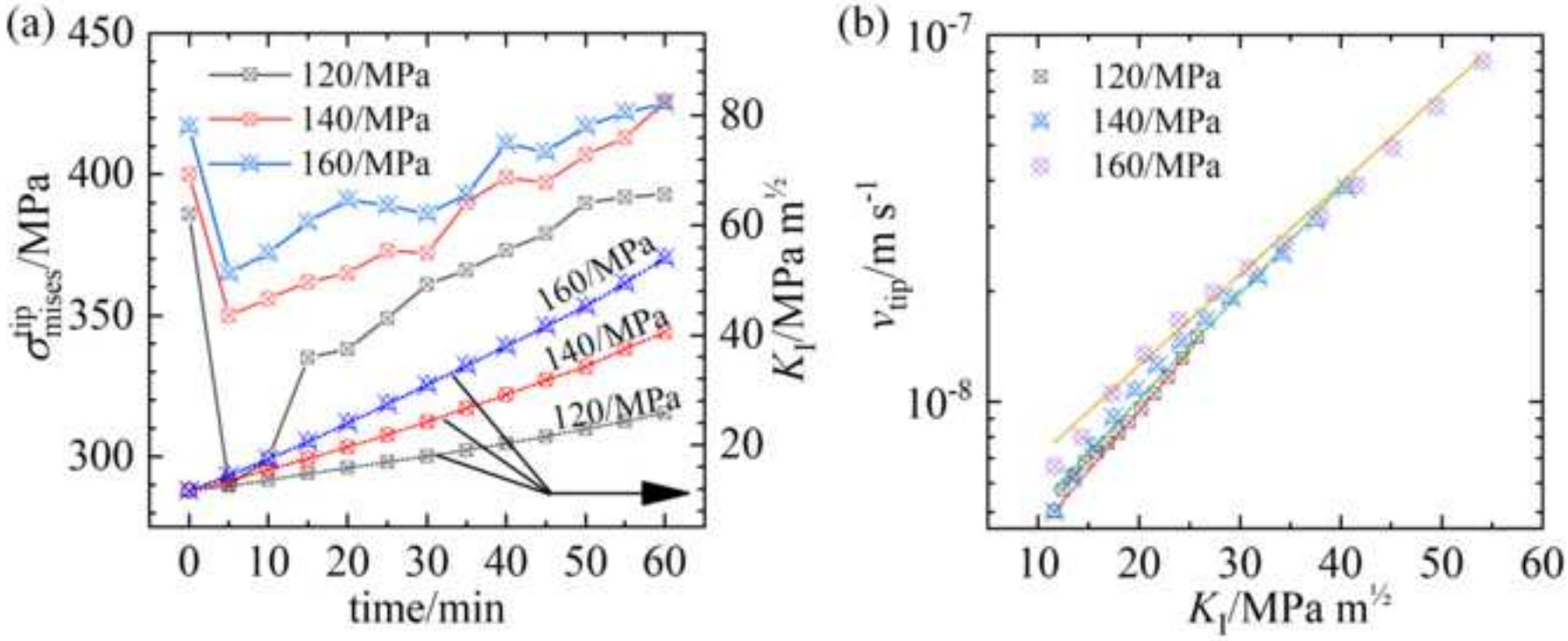

Figure 08

Click here to access/download;Figure(s);fig. 08.tif

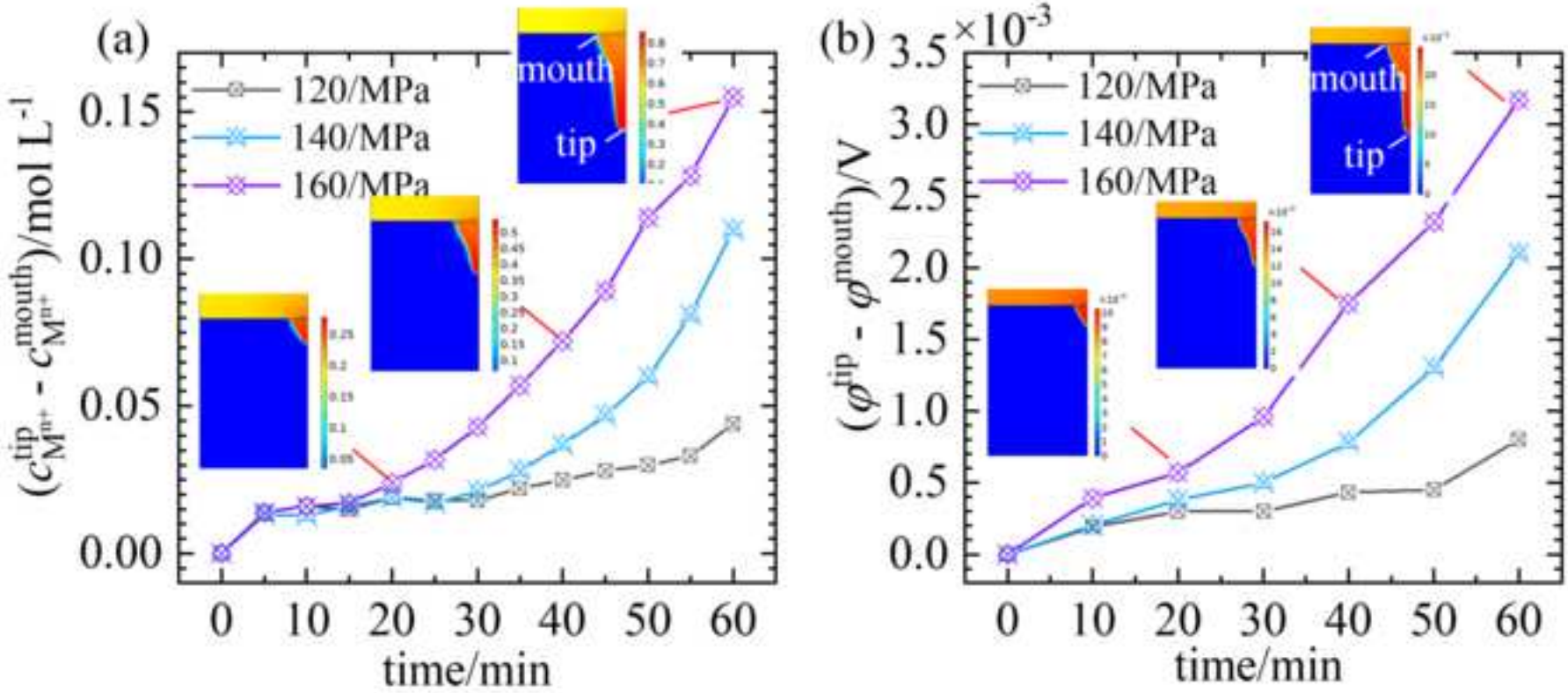

Figure 09

Click here to access/download;Figure(s);fig. 09.tif

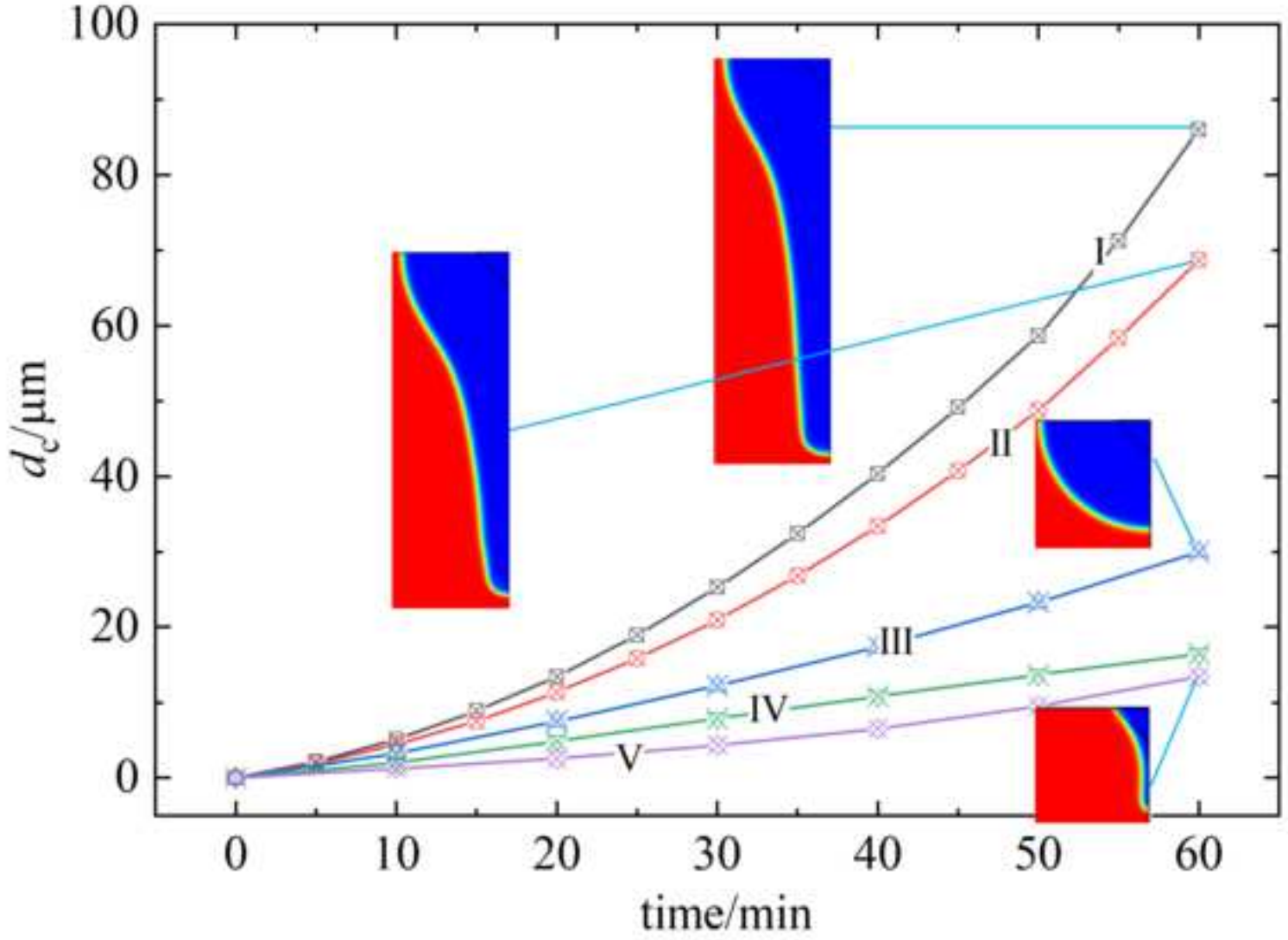

Figure 10

Click here to access/download;Figure(s);fig. 10.tif

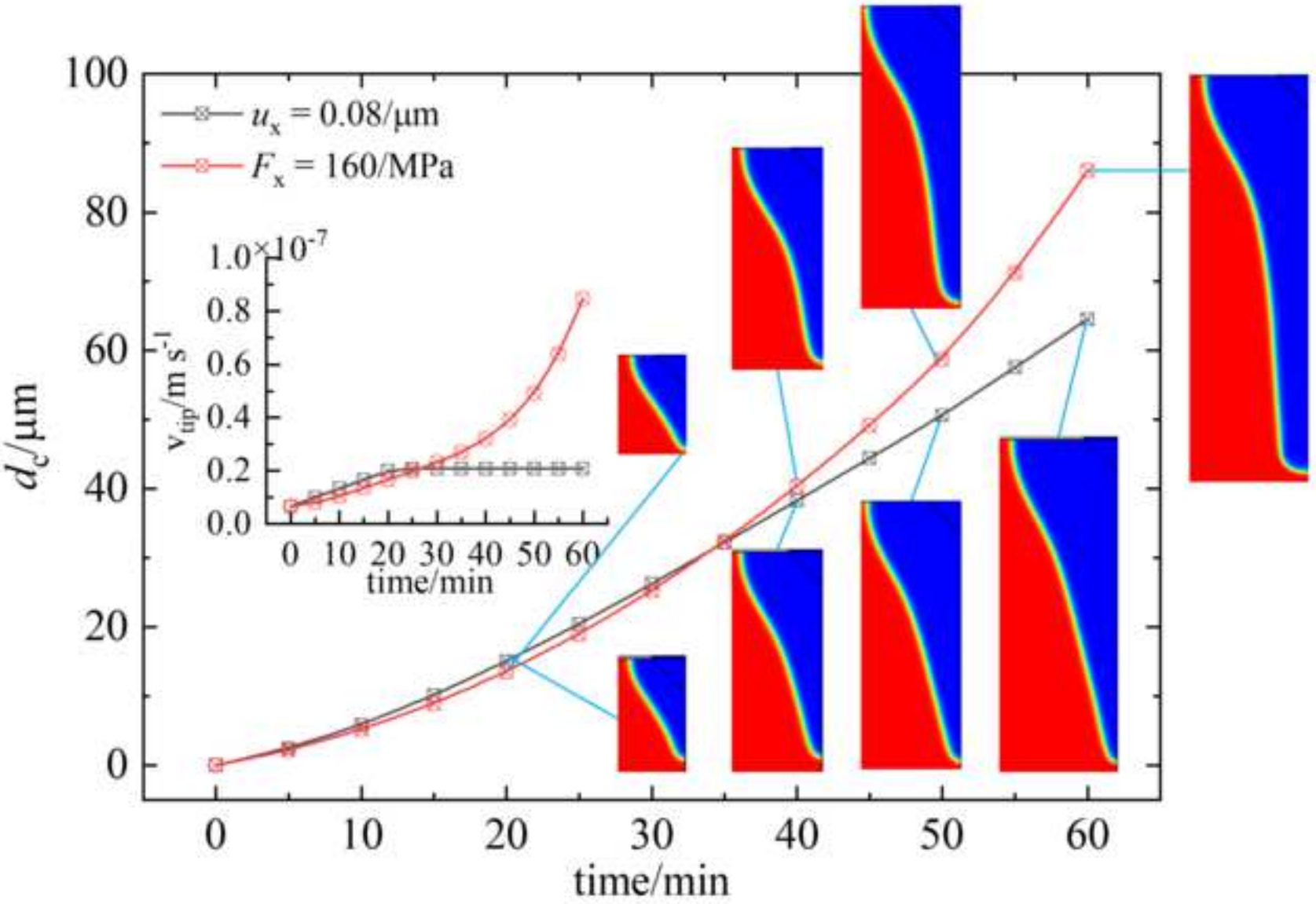

Figure 11

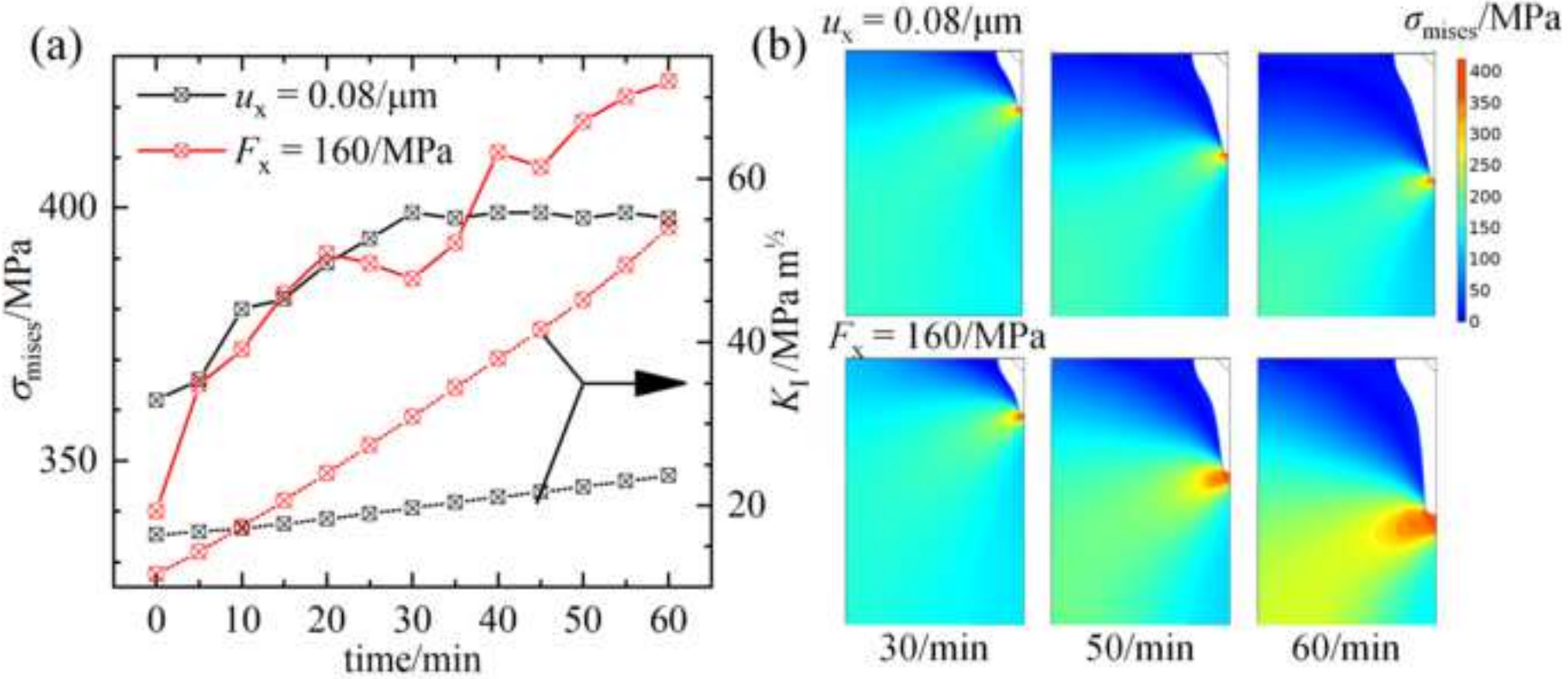

Figure 12

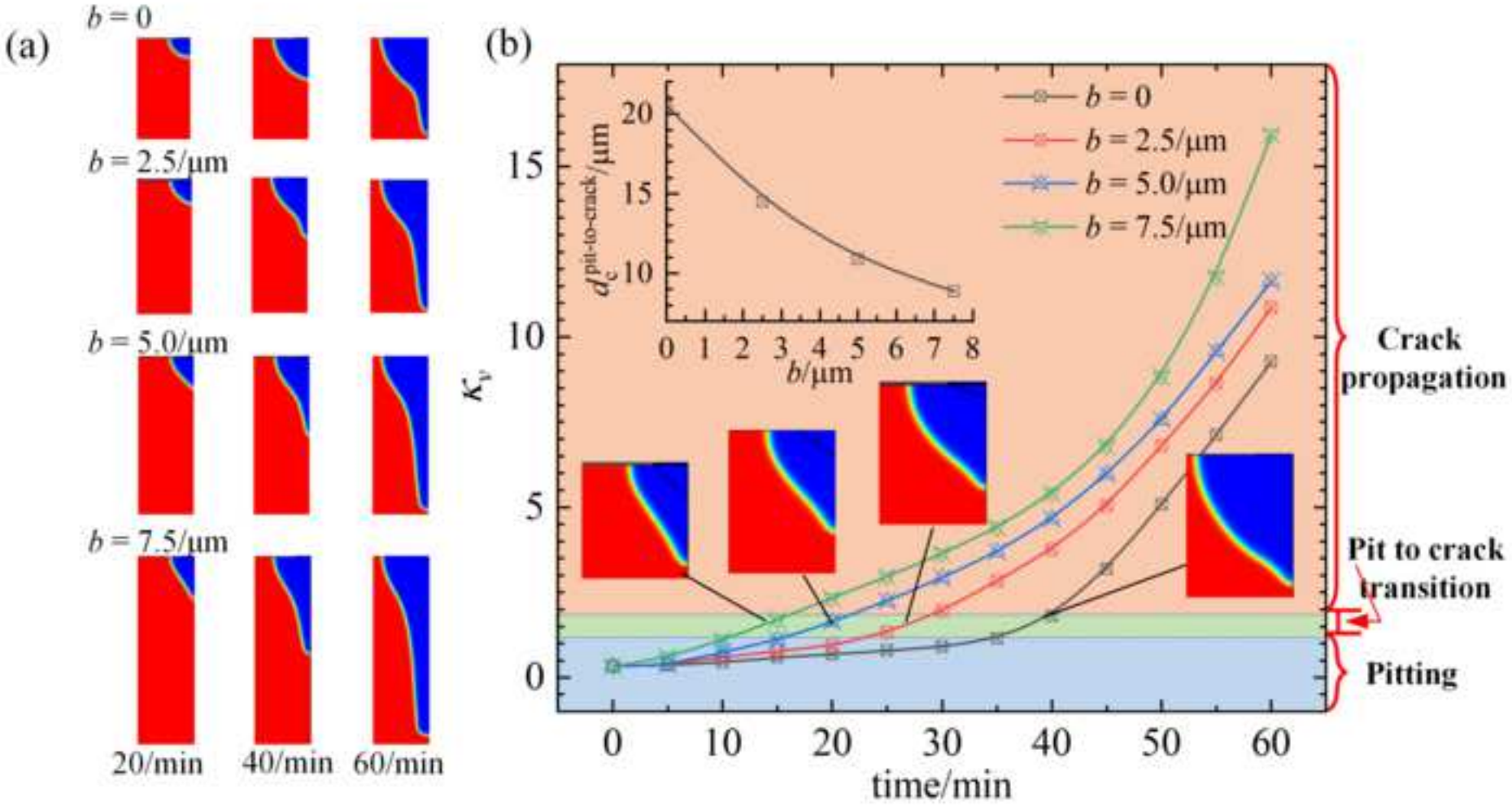

Figure C.1

Click here to access/download;Figure(s);fig. C.1.tif

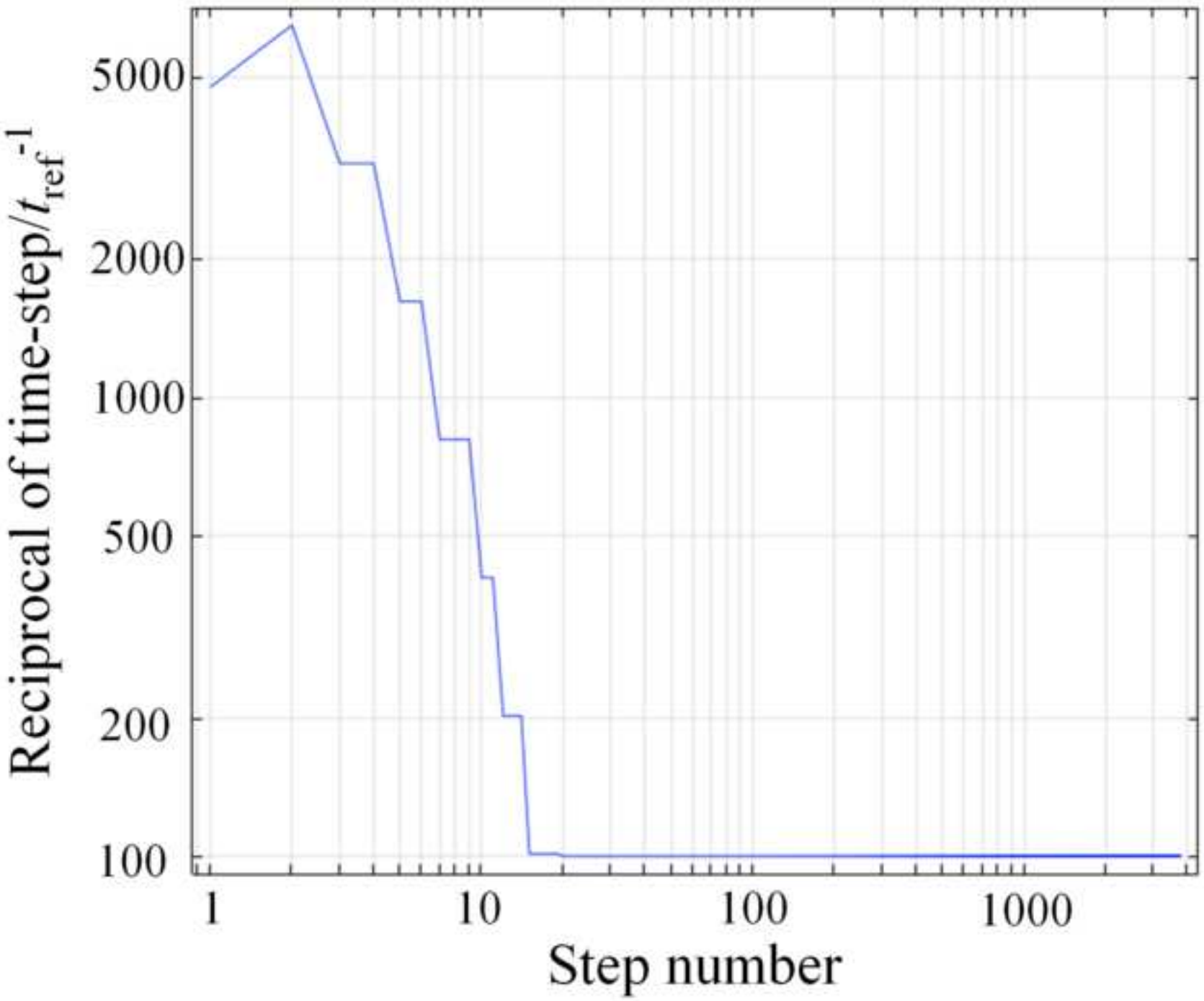

Highlights

- A mechano-chemical coupling model is proposed to study SCC
- The critical condition of pit-to-crack transition is unveiled
- The accelerated cracking due to the interplay of stress and corrosion is predicted
- The variation of electrochemical environment near a crack tip is predicted
- The effects of initial stress state and pit geometry are evaluated

Certificate of language editing